

# A comparison of model-scale experimental measurements and computational predictions for a large transom-stern wave

David A. Drazen<sup>1</sup>, Anne M. Fullerton<sup>1</sup>, and Thomas C. Fu<sup>1</sup>  
Kristine L.C. Beale<sup>2</sup>, Thomas T. O’Shea<sup>2</sup>, Kyle A. Brucker<sup>2</sup>,  
Douglas G. Dommermuth<sup>2</sup>, and Donald C. Wyatt<sup>2</sup>  
Shanti Bhushan<sup>3</sup>, Pablo M. Carrica<sup>3</sup>, and Fred Stern<sup>3</sup>

<sup>1</sup>Naval Surface Warfare Center - Carderock, USA

<sup>2</sup>Science Applications International Corporation, USA

<sup>3</sup>University of Iowa, USA

## ABSTRACT

The flow field generated by a transom stern hullform is a complex, broad-banded, three-dimensional system marked by a large breaking wave. This unsteady multiphase turbulent flow feature is difficult to study experimentally and simulate numerically. Recent model-scale experimental measurements and numerical predictions of the wave-elevation topology behind a transom-sterned hullform, Model 5673, are compared and assessed in this paper. The mean height, surface roughness (RMS), and spectra of the breaking stern-waves were measured by Light Detection And Ranging (LiDAR) and Quantitative Visualization (QViz) sensors over a range of model speeds covering both wet- and dry-transom operating conditions. Numerical predictions for this data set from two Office of Naval Research (ONR) supported naval-design codes, Numerical Flow Analysis (NFA) and CFDship-Iowa-V.4, have been performed. Comparisons of experimental data, including LiDAR and QViz measurements, to the numerical predictions for wet-transom and dry transom conditions are presented and demonstrate the current state of the art in the simulation of ship generated breaking waves. This work is part of an ongoing collaborative effort as part of the ONR Ship Wave Breaking and Bubble Wake program, to assess, validate, and improve the capability of Computational Fluid Dynamics (CFD).

## INTRODUCTION

The flow field generated by a transom stern hullform is a complex system dependent upon a number of variables, including the transom height and shape, buttock slope, the wave system generated upstream, the boundary layer flow around the hull, etc., and has been the subject of a number of studies. While earlier work has focused on the

surface wave profile (Maki, Doctors & Beck 2007, for example), detailed laboratory scale measurements of the flow field have been performed by Lasheras (Rodríguez-Rodríguez, Marugán-Cruz, Aliseda & Lasheras 2008), who focused on identifying the general flow topology. More recently, the development of advanced instrumentation has allowed for measurement of the breaking transom wave of a full-scale ship to be made (Fu, Fullerton, Terrill & Lada 2006a). In an associated effort, numerical predictions of the full-scale stern wake and comparisons of the mean height, surface roughness (RMS), and spectra of the breaking stern-waves were made (Wyatt, Fu, Taylor, Terrill, Xing, Bhushan, O’Shea & Dommermuth 2008). Although these initial comparisons of the numerical predictions and full-scale measurements showed generally good agreement, differences remained that were difficult to associate with the underlying phenomenology due to the complexities of in-situ collection.

To obtain quantitative breaking wave data from a large-scale transom stern hull form, measurements of the free-surface elevation in stern region of a large transom model were made in June of 2007 (Fu, Fullerton, Ratcliffe, Minnick, Walker, Pence & Anderson 2009b) and October/November of 2008 (Fu, Fullerton, Drazen, Minnick, Walker, Ratcliffe, Russell & Capitain 2010). This large-scale laboratory experiment provides a more canonical transom wave for study, removing the effects of the propellers, appendages, and ambient conditions. For this experiment a large, specially designed transom stern model was developed and tested in the Naval Systems Warfare Center - Carderock (NSWCCD) Carriage 2 Towing Tank. The hullform used, Model 5673, was purpose-built for these experiments. It was designed to provide a minimal bow-wave disturbance and maximum stern-wave disturbance. Its dimensions were determined by the maximum practical size allowable in the Carriage 2 facility. Her hull construction was fiberglass. A schematic of Model 5673 is shown in Figure 1, and the

vessel geometry is detailed in Table 1. The experiment and data reduction and analysis are described in the Experimental Measurements section of this paper.

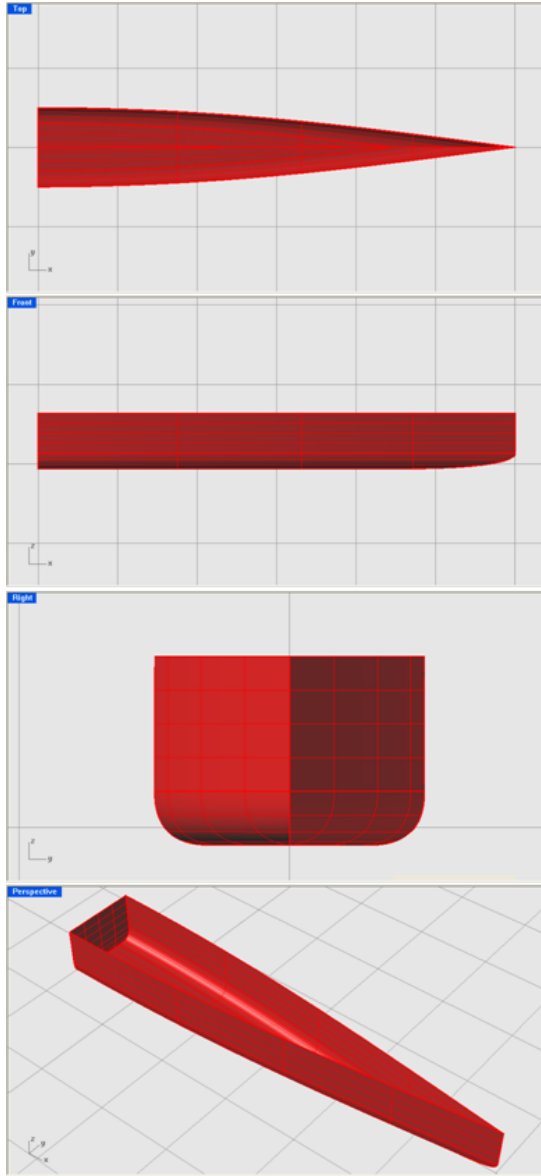


**Figure 1:** Model 5673. Rendered at scale. Grid line separation is 1.524 m (5').

The model-scale measurement data is compared to predictions from two Computational Fluid Dynamics (CFD) codes currently under development by the Office of Naval Research (ONR), Numerical Flow Analysis (NFA) and CFDship-Iowa-V.4. NFA is a Cartesian grid formulation of the Navier-Stokes equations utilizing a cut-cell technique to impose the hull boundary conditions (Dommermuth, O’Shea, Wyatt, Ratcliffe, Weymouth, Hendrikson, Yue, Sussman, Adams & Valenciano 2007, O’Shea, Brucker, Dommermuth &

Table 1 Model 5673 Details

Length Overall, $L_o$	9.144 m (30 ft)
Waterline Length	9.144 m (30 ft)
Extreme Beam	1.524 m (5 ft)
Bow Draft	Fixed
Stern Draft, $T_{max}$	Variable
Construction	Fiberglass
Displacement	771.1 kg (1700 lb)

Wyatt 2008, Brucker, O’Shea, Dommermuth & Adams 2010). CFDship-Iowa-V.4 is an unsteady Reynolds-Averaged Navier-Stokes (URANS)/detached eddy simulation (DES) code that uses a single-phase level-set method, advanced iterative solvers, conservative formulations, and the dynamic overset grid approach for free surface flows (Bhushan, Xing, Carrica & Stern 2007). The two CFD techniques are compared in separate but complimentary sections in the Numerical Predictions portion of this paper.

## EXPERIMENTAL MEASUREMENTS

The initial experiment, conducted in 2007, was designed to enable the examination of the transom-stern wake transition from fully wet to fully dry and focused on obtaining mean wave field data. Table 2 lists the test conditions. Four speeds [2.57, 3.60, 4.12, and 4.63 m/s (5,7,8, and 9 knots)] were tested. During the experiment the transition from a wet to dry transom was observed to occur between 3.60 and 4.12 m/s (7 and 8 knots). The follow on phase, conducted in 2008, focused on collecting a more detailed data set at the Froude numbers which straddle the wet/dry transom condition. The model was statically ballasted to the same waterline in 2007 and 2008, with a transom submergence of 0.305 m, as shown in Figure 2. A view of the transom stern wake at each of the Froude numbers tested is given in Figure 3. A variety of instrumentation was deployed to characterize the transom wake field. A summary of the experimental work will be described herein, further specifics can be found in Fu et al. (2009b) and Fu et al. (2010). The discussion in this paper will focus on the surface elevation measurement results from runs at 3.60 (7 knots) and 4.12 m/s (8 knots) due to the large volume of data collected at these speeds.

### *Light Detection and Ranging (LiDAR)*

The free-surface deformation was measured using a scanning Light Detection And Ranging (LiDAR) system. The LiDAR system used at NSWCCD, Riegl LMS-Q140-80i (Fu, Rice, Terrill, Walker & Lada 2006b, Fu,

Table 2 Calculated trim angle and draft for the 2007 and 2008 data. The Froude numbers based on ship length and draft are  $F_{r_L}$  and  $F_{r_{Tmax}}$  respectively.  $R_{e_L}$  is the Reynolds number based on ship length.

Speed m/s	Speed knots	Test Yr.	$F_{r_L}$	$R_{e_L}$	Trim (deg)	$T_{FP}$ (m)	$T_{AP}$ (m)	$F_{r_{Tmax}}$	Transom Condition
2.57	5	'07	0.27	$2.35 \cdot 10^7$	0.19	0.296	0.323	1.43	Wet
3.60	7	'07	0.38	$3.29 \cdot 10^7$	0.51	0.284	0.366	1.9	Wet
3.60	7	'08	0.38	$3.29 \cdot 10^7$	0.48	0.287	0.363	1.91	Wet
4.12	8	'07	0.43	$3.77 \cdot 10^7$	0.73	0.274	0.366	2.1	Dry
4.12	8	'08	0.43	$3.77 \cdot 10^7$	0.67	0.277	0.384	2.12	Dry
4.63	9	'07	0.49	$4.23 \cdot 10^7$	0.78	0.274	0.393	2.34	Dry

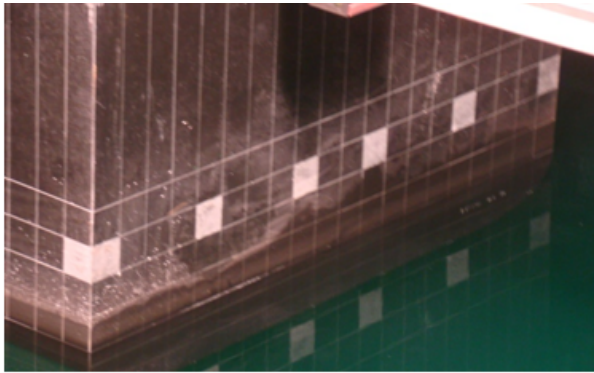


Figure 2: The initial submergence of the transom in 2007 and 2008 was 0.305 m

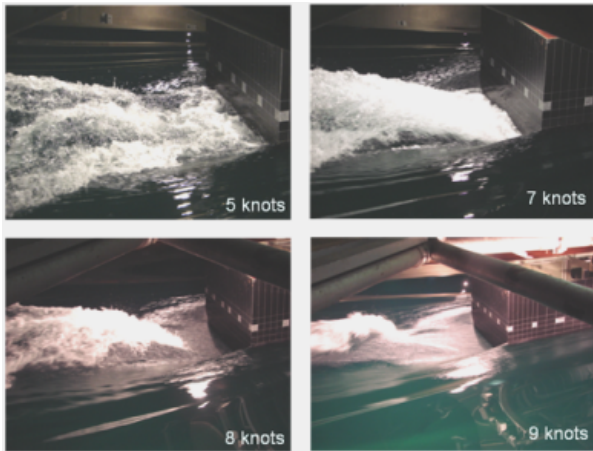


Figure 3: A series of still images collected at each speed tested. Only results from speeds of 3.60 m/s (7 knots) and 4.12 m/s (8 knots) will be discussed.

Fullerton & Drazen 2009a), has a range accuracy of  $\pm 2.54$  cm for highly reflective surfaces. The instrument scans an angular region of  $\pm 40^\circ$  at a maximum line sample rate of 40 Hz with a maximum laser pulse frequency of 30 kHz. As infrared radiation is absorbed by water, only a small fraction of the incident energy is scattered back to the instrument.

The LiDAR system was mounted to a traverse which moved in a direction parallel to the centerline of the model, on a pan and tilt unit which allowed for remote control of the LiDAR's position during testing. In 2007 the traverse was located 3.87 m above the mean waterline and 0.25 m starboard of centerline. In 2008 the traverse was at an elevation of 4.82 m and was 0.143 m port of centerline.

The primary goal of the LiDAR system's measurements during the 2007 test period was to capture the gross properties of the transom stern wake. Data was collected at a number of discrete locations aft of the transom at a line sampling rate of 20 Hz. During the 2008 test period the focus was on capturing the statistical properties (mean and standard deviation) of the transom stern wake with the LiDAR. A set of three fixed locations aft of the transom were selected and multiple runs were made at a line sampling rate of 20 and 40 Hz. This data will be referred to as the fixed LiDAR data. Additional tests were conducted in 2008 where the LiDAR was driven down the traverse at a constant speed of 3.70 cm/s with a sampling rate of 20 Hz, yielding a map of the surface elevation with an inter-line spacing of 2 mm. The surface map extended from 0.422 m to 2.19 m aft of the stern in one run. This data will be referred to as the moving LiDAR data set. A summary of the discrete locations measured by the LiDAR during both testing phases is given in Table 3 and is also shown in Figure 4.

The LiDAR returns a measurement of the distance to the free-surface and the data was first corrected to yield elevation above the mean water level (MWL). The MWL was computed each day during the testing. For each measurement point the elevation, spatial location along

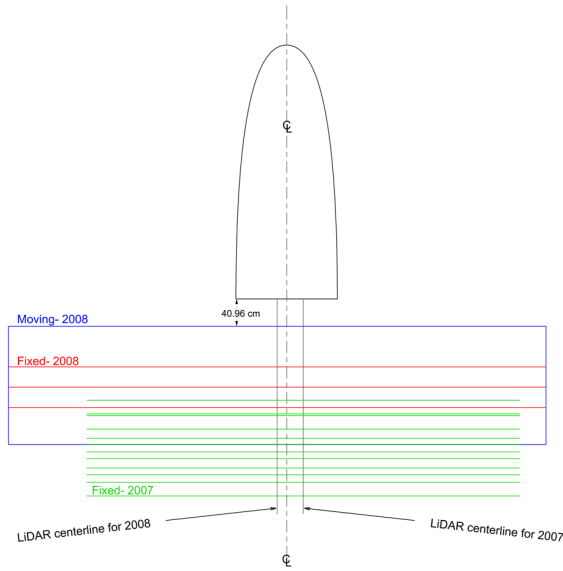


**Figure 4:** Schematic showing the location of the LiDAR measurements in 2007 and 2008. The field of view for the 2008 fixed and moving LiDAR measurements are shown as red and blue lines. The locations of the fixed LiDAR data from 2007 are shown in green. Not all measurement locations aft of the transom were shown for 2007 due to the close spacing between lines. All scan line widths are theoretical maximums. See Table 3 for specific distances.

the line, elevation above the MWL, and return signal strength (i.e., amplitude) was returned. Any point where the amplitude of the return signal was 0 was ignored during subsequent processing by setting it to be a NaN (Not a Number). As the LiDAR has a constant angular step between measurement points, the spacing between adjacent measurements increases away from the centerline. In order to correct for this, the data was binned and the average of all points within the bin returned. For the 2007 data the bin spacing was 2 cm and 5 cm for the 2008 data.

The fixed LiDAR measurements of the mean and standard deviation of the transom wake at 3.60 m/s and 4.12 m/s (7 and 8 knots) from 2008 are shown in Figure 5 and Figure 6. The mean and standard deviation of the signal strength is also shown, as the standard deviation could be affected by a large variability in the measured signal strength. The large elevation spike seen at  $\approx 89$  cm is caused by the LiDAR reflecting off of the traverse supporting the Quantitative Visualization (QViz) system. The large RMS values between  $Y = 0.4 - 0.7$  are likely due to the QViz camera system moving within the field of view of the LiDAR. At a speed of 4.12 (8 knots) the standard deviation of the elevation is seen to increase

Table 3 Fixed locations aft of the transom where stationary LiDAR measurements were taken during 2007 and 2008. See Figure 4 for a schematic of the LiDAR coverage area.

Speed (knots)	5	7	7	8	8	9
Test Year	'07	'07	'08	'07	'08	'07
1.019 m			X		X	
1.324 m			X		X	
1.519 m	X	X		X		X
1.629 m			X		X	
1.723 m	X	X		X		X
1.748 m	X	X		X		X
1.951 m	X	X		X		X
1.964 m		X				
2.091 m						X
2.180 m	X	X		X		X
2.193 m	X					X
2.294 m		X				
2.396 m	X	X		X		X
2.536 m		X		X		
2.637 m	X	X		X		X
2.752 m		X		X		
2.955 m						X

Table 4 Total amount of data used to generate the mean and standard deviations shown in Figure 5 and 6. These represent concatenations of approximately three to six separate runs.

Speed m/s	Speed (knots)	$x$ Position		
		1.019 m	1.324 m	1.629 m
3.60	7	202 s	321 s	318 s
4.12	8	137 s	192 s	119 s

along the shoulder consistent with the reduction in signal strength as one moves away from the transom centerline.

The results shown in Figures 5 and 6 were computed from data collected at sample rates of both 20 and 40 Hz, see Table 4 for the total amount of data collected in 2008. The sampling rate was varied in order to obtain a mixture of improved spatial and temporal resolution.

Collection of the moving LiDAR data was a secondary goal of the test and therefore the volume of data is much less when compared to the fixed LiDAR case. There are three individual runs at a speed of 3.60 m/s (7 knots) and five individual runs at a speed of 4.12 m/s (8 knots). Each run was started individually and therefore each run had to be aligned during post-processing. After each individual run was re-aligned, the mean el-

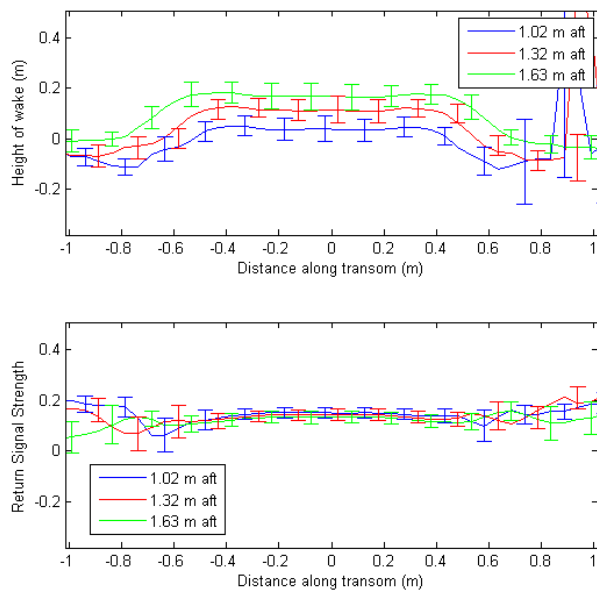


**Figure 5:** LiDAR measurements at three fixed locations aft of the transom for a speed of 3.60 m/s (7 knots). The data was collected in 2008 and was binned with a bin size of 5 cm. The mean and standard deviation of the wake elevation are shown in the top figure. The mean and standard deviation of the return signal strength is shown in the bottom figure.

ewation from the moving LiDAR was compared against the fixed LiDAR data to insure that no mis-alignment had occurred. The LiDAR results from 2008 is shown in Figure 7. RMS values are not shown for the moving case due to the small sample size.

Frequency spectra were computed along the centerline at the three fixed aft locations measured in 2008. They are shown in Figure 8. Peaks in the spectra near 2 Hz are evident in the 3.60 m/s (7 knots) dataset (shown by a dashed line) for all distances aft of the transom. This phenomena is thought to be related to the shedding of vortices off the transom and was also seen by Wyatt et al. (2008). The peak is seen to vanish at a speed of 4.12 m/s (8 knots) when the transom becomes fully ventilated and would be consistent with a process driven in part by vortex shedding. Wyatt et al. (2008) also describe this result as a possible generation mechanism and suggest that it could also be due to waves which interact after having propagated off of the transom corner. A scaling of the Strouhal number between the model and full-scale Athena measurements predicts a peak between 1.7-2.4 Hz based on a transom submergence of  $\approx 18.5$  cm at 3.60 m/s (7 knots), consistent with the vortex shedding hypothesis.

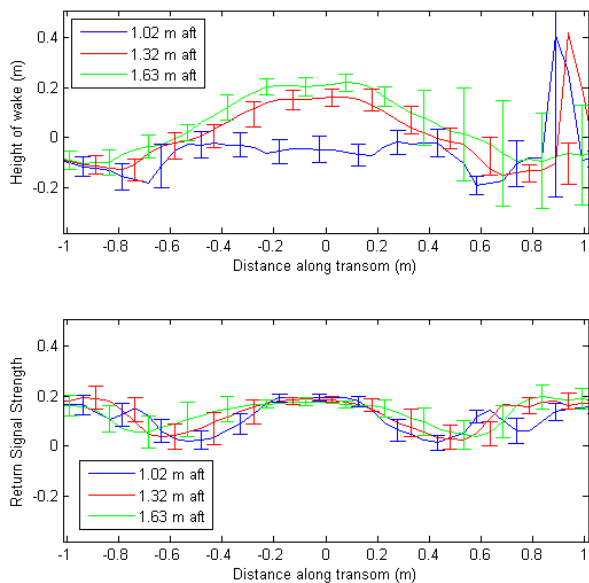


**Figure 6:** LiDAR measurements at three fixed locations aft of the transom for a speed of 4.12 m/s (8 knots). The data was collected in 2008 and was binned with a bin size of 5cm . The mean and standard deviation of the wake elevation are shown in the top figure. The mean and standard deviation of the return signal strength is shown in the bottom figure.

### Quantitative Visualization (QViz)

Free-surface elevation measurements of the breaking wave were obtained by an optical laser sheet QViz system (Furey & Fu 2002). These measurements represent an effort to capture the statistical properties of the near-hull wake region, where accessibility is difficult by alternate sensors, and to evaluate the dynamics across the wake shoulder into the breaking region. Shown schematically in Figure 9, the QViz system collected digital images of the intersection of the breaking transom wave with a laser light sheet, projected parallel to the transom edge, to generate lateral free-surface profiles for a systematic set of axial positions. Subsequent image processing has been completed to transform the resulting wave shape from pixels in the image plane into world coordinates.

The major components of the Qviz system deployed during this experiment are depicted in Figure 10. A laser beam produced by a 3 watt laser with 532 nm wavelength was fed through a fiber-optic cable to an enclosed housing containing a cylindrical lens. The beam was then converted by the lens into a light sheet which was projected perpendicular to the disturbed free-surface. Digital images of the resulting deformed light at the intersection were acquired by two progressive scan non-interlaced video cameras (JAI model CV-A11) operating at 30 frames per second, and lenses (Computar model

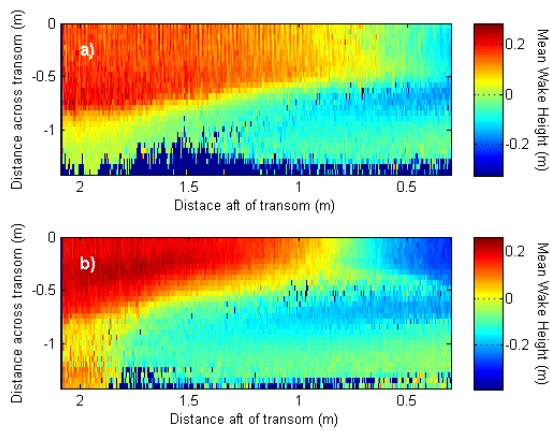


**Figure 7:** a) Surface map of transom wake elevation generated from mean of three LiDAR runs collected in 2008 at a speed of 3.60 m/s (7 knots). b) Surface map of transom wake elevation generated from mean of five LiDAR runs collected in 2008 at a speed of 4.12 m/s (8 knots).

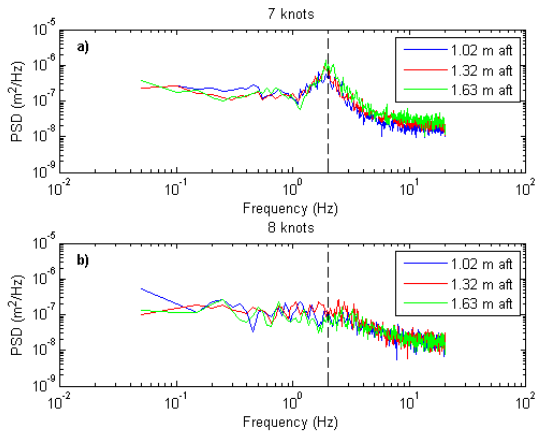


**Figure 8:** Frequency power spectra of LiDAR measurements at three fixed locations aft of the transom for a speed of a) 3.60 m/s (7 knots) and b) 4.12 m/s (8 knots). The data was collected in 2008 and three adjacent measurements along the centerline were averaged after computing the spectrum. The vertical dashed line is the location of the spectral peak seen in the 3.60 m/s (7 knots) data.

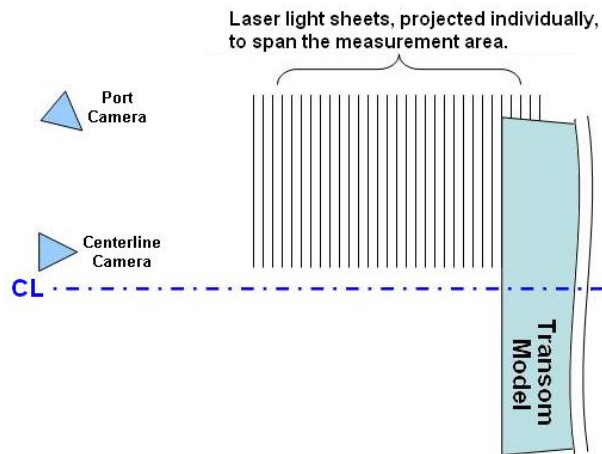


**Figure 9:** Schematic representation of the QViz system: two cameras captured images of the intersection between the wave field generated by the transom and systematic laser light sheets, projected as transverse lines, from a cylindrical lens.

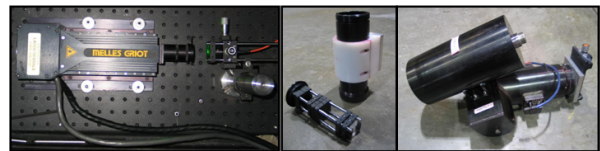


**Figure 10:** Major QViz system components: laser as directed into a fiber-optic cable (left), cylindrical lens assembly and housing (center), and a camera housed in a motorized pan and tilt unit (right).

H6Z0812M) fitted with 532 nm filters to reduce ambient light noise. The cameras were housed by Applied Microvideo pan and tilt units mounted to an optical rail system, along with the lens housing. The rail assembly was moved, in fixed increments, longitudinally aft of the model by a motorized traverse, shown in Figure 11.

The QViz system successfully acquired cross-sections of the flow at 3.6 m/s (7 knots) spanning roughly 0.1270 to 0.7874 meters to port of the model centerline for axial locations spaced every 0.0254 meters from 0.0254 to 0.6604 meters aft of the transom and every 0.0508 meters from 0.6604 to 1.2192 meters aft. The measurements of the flow at 4.12 m/s (8 knots) spanned roughly from centerline to 0.8128 meters to port, and axially from 0.0254 to 0.1524 meters at 0.0254 meter increments, and at 0.0508 meter increments from 0.1524 to 1.2192 meters aft of the transom. The resolution of the images for this experiment was on the order of 1 millimeter.

The images were each processed using a matched filtering approach to define the edge acquired at each instant. This algorithm and its capabilities are described in

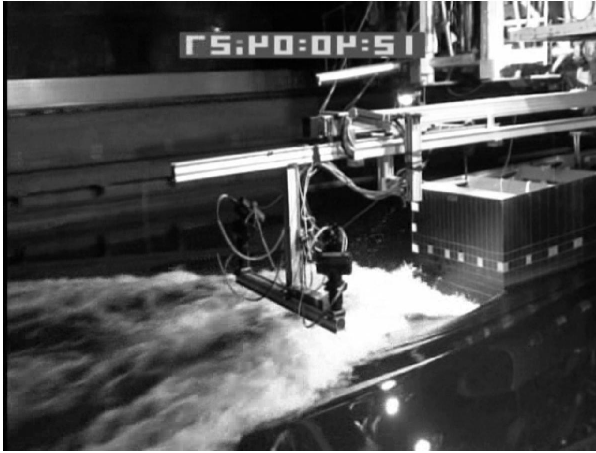


**Figure 11:** Photograph of the QViz transverse as mounted during the 2008 Transom Experiment.

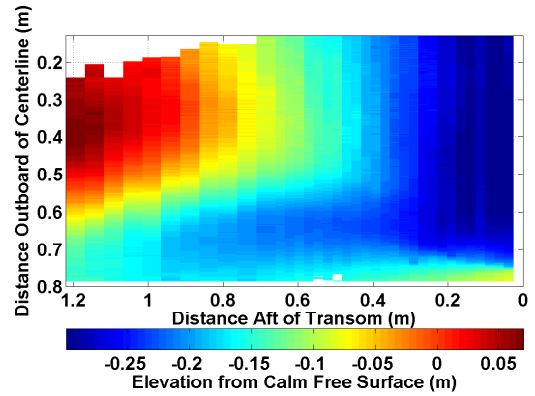
detail in Beale, Fu, Wyatt & Walker (2010). For processing of the 2008 data, a single impulse response was used to determine the matched filter output for each image obtained from both cameras and for both model speeds. The selected impulse response was generated by pre-processing each run to determine the edge detector with the maximum ratio of half-height to half-width, and averaging each of these for all runs. The resulting matched filter output was thresholded using a value of three times the standard deviation as a false alarm cutoff.

The complex free-surface elevation and its roughness have been determined by binning the calibrated edge detection results of both cameras. The QViz elevation fields are shown in Figure 12 for model speeds of 3.6 m/s (7 knots) and 4.12 m/s (8 knots).

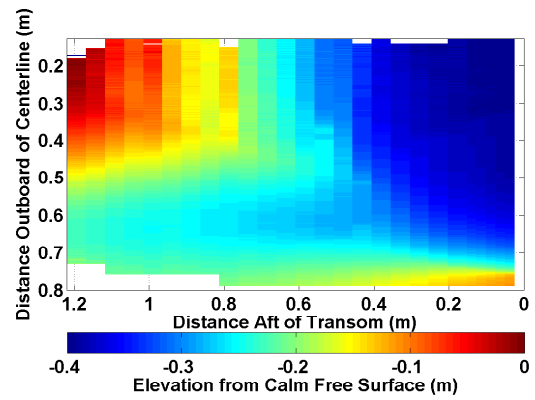
The frequency content, as measured by the QViz technique for individual time series, have also been examined. Previous versions of this technique have been successfully employed to obtain full-scale field measurements of ship generated waves (Furey & Fu 2002, Rice, Walker, Fu, Karion & Ratcliffe 2004), as well as laboratory breaking bow waves (Karion et al. 2003). The production of meaningful spectral content, however, is a new capability resulting from the matched filtering processing scheme.

#### *Senix Ultrasonic Sensors*

The Senix Corporation's ToughSonic® Ultrasonic sensor is a non-contact, acoustic instrument for measuring distances through air. A number of these were deployed during the 2007 and 2008 phases of the testing for the collection of longitudinal wavecut data. In 2008 a single Senix sensor was used to supplement measurements of the transom wake elevation. The sensor was mounted to the QViz traverse and approximately 10 sec-



(a)



(b)

**Figure 12:** Transom wake elevations generated from QViz measurements, for model speeds of (a) 3.6 m/s (7 knots) and (b) 4.12 m/s (8 knots).

onds of data were collected at 20 Hz at a number of static locations aft of the stern. The traverse was also moved longitudinally at a steady speed in order to obtain a profile of the wake. The sensor was located 8 mm starboard of the model centerline, and was traversed from the stern to 1.134 m aft of the stern.

The data was processed to yield maximum and minimum elevations as well as mean and standard deviations of the wake elevations. Multiple measurements at the same fixed location were averaged to obtain a single value. The data from the moving ultrasonic sensor was binned into 2.5 cm increments and then averaged for each bin reported. No data was reported for the 4.12 m/s (8 knots) case within 0.508 m of the transom as the water level was outside the calibrated range of the instrument. The results for 3.60 m/s (7 knots) and 4.12 m/s (8 knots) are shown in Figure 13.

#### *Void Fraction Measurements*

A set of six impedance void fraction probes were used to measure the fraction of air entrained in the tran-

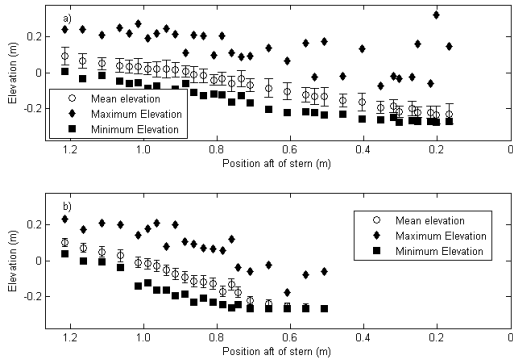


**Figure 13:** Centerline ultrasonic measurements at 3.60 m/s (7 knots) (a) and 4.12 m/s (8 knots) (b). Positions aft are referenced to stern at 0 cm. There is no data forward of 0.508 cm for the 8-knot case as the water level was outside of the calibrated range.

som stern wake. Data was collected in both 2007 and 2008, with reduced noise in the 2008 measurements due to improved electronics (Waniewski 1999). The probes consist of two concentric stainless steel electrodes separated by insulation. The outer electrode is grounded and a sinusoidal voltage of  $\pm 2.5$  V with an excitation of 500 kHz is applied to the inner electrode. The impedance across the two electrodes increases with increased void fraction and is mainly resistive for excitation frequencies below the megahertz level. When an air bubble is pierced by a probe, the current between the two electrodes decreases and voltage output of the probe is a large negative spike. The sampling rate of the probes was set at 20 kHz and was determined based on the limitations of the data acquisition system. See Fu et al. (2009b) and Fu et al. (2010) for further details on the setup of the probes.

The probes were mounted in a brass strut with a vertical separation of 8.9 cm. The vertical position of the strut relative to the mean water level could be adjusted and data was collected at three locations, yielding a final vertical resolution of 4.4 cm. In 2007, data was collected at 3.60 m/s (7 knots) at four longitudinal locations aft of the transom: 0.53 m, 0.66 m, 0.79 m, and 0.91 m. At 4.12 m/s (8 knots), data was collected at 1.04 m, 1.17 m, 1.29 m, and 1.42 m aft of the transom. Between two to three runs were collected at each position for both speeds and the results were then averaged. Error analysis can be found in Appendix A of Fu et al. (2009b). Data was collected in 2008 at seven longitudinal locations aft of the transom (1.04 m, 1.10 m, 1.17 m, 1.29 m, 1.36 m, 1.42 m, and 1.48 m) for 4.12 m/s (8 knots) only. Due to issues with noise when all six probes were operating, only two or three probes were used at a time during the 2008 test period. Results for 3.60 m/s (7 knots) from 2007 and 4.12 m/s (8 knots) from 2007 and 2008 are in

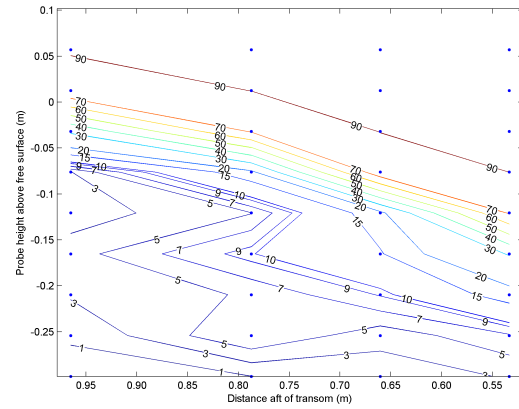


**Figure 14:** Contour plot of void fraction measurements taken in 20087 at a speed of 3.60 m/s (7 knots). The measurement locations are denoted by blue dots.

Figures 14 and 15, respectively. The spacing of contour lines was chosen based on the largest error for a given void fraction range. The contour plots agree qualitatively well with observations made from images of the transom wake. The spikes in Figure 15 at (1.1 m, -0.076 m) and (1.17 m, -0.159 m) are thought to be the result of the crude merging of the 2007 and 2008 datasets. Comparison of results from 2008 and 2007 seem to indicate that the data point at (1.36 m, 0.013 m) might be an outlier, possibly due to noise in the system.

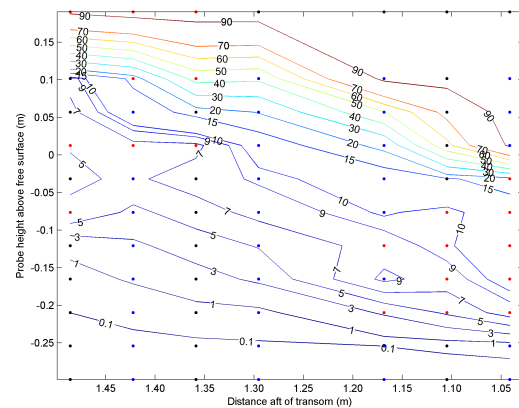


**Figure 15:** Contour plot of void fraction measurements taken in 2007 and 2008 at a speed of 4.12 m/s (8 knots). The blue dots represent the 2007 data, the red dots 2008 data, and the black dots are the results of linear interpolation between 2007 and 2008 results.



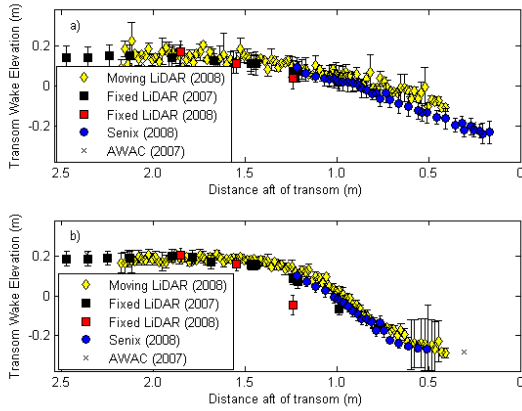


**Figure 16:** A comparison between measurements of the transom wake elevation from a variety of instruments used in 2007 and 2008. The symbols are the mean values and the errorbars represent the standard deviation of the measured data.

#### *Other Measurements*

The velocity field within the wake was measured using a Nortek Acoustic Wave and Current (AWAC) profiler and SonTek® Acoustic Doppler Velocimeter (ADV®) (YSI Incorporated). The AWAC profiler measured velocity and acoustic backscatter in the water column while the ADV measured water velocity only. An estimate of the free-surface deformation was also available from the AWAC profiler see Fullerton & Fu (2003). Defocused Digital Particle Image Velocimetry (DDPIV), (Pereira, Gharib, Dabiri & Modarress 2000, Jeon, Pereira & Gharib 2003), was used to measure the bubble size distribution at a fixed depth aft of the transom. Video measurements of the flow field aft of the transom were made with both standard and high-speed video cameras. For the high-speed video data, a fluorescent dye was injected at the transom as a tracer.

#### EXPERIMENTAL MEASUREMENTS DISCUSSION

All of the instrumentation used to quantify the free-surface is non-intrusive. The main difficulty in interpreting the data is in determining which surface each instrument is actually measuring. A comparison between the LiDAR measurements, centerline ultrasonic data, and AWAC data from both 2007 and 2008 is shown in Figure 16.

All measurements agree qualitatively well up to  $\approx 150$  cm aft of the transom. Beyond this point, the LiDAR data begins to diverge from the ultrasonic and AWAC results. This is likely caused by a reduction in the returned signal strength as the number of scatters at the water surface decreases, i.e., less surface roughness. The good qualitative agreement indicates that all instru-

ments appear to be measuring the same surface. Which surface this corresponds to is unknown and remains an important question to be answered.

When using infrared instrumentation, registration of the exact measurement location relative to a fixed origin is often difficult. An initial 0.41 m offset was applied to the LiDAR data presented here. Comparisons of 2008 LiDAR measurements to other measurements that are not shown, including 2007 LiDAR measurements and 2007 and 2008 longitudinal wave cuts, suggest that the 2008 LiDAR measurements are not registered properly in the longitudinal direction. At one point during the 2008 test period, the forward attachment point on the model came loose and the model moved from its original position. An attempt was made to place it back in its original position, but this could account for some of the identified offset. Work is currently underway in an attempt to identify the magnitude of the offset and any possible causes.

#### NUMERICAL PREDICTIONS

Initial comparisons of the experimental measurements are made to predictions from NFA and CFDship-Iowa-V.4 in the following sub-sections. Comparison of the 2008 LiDAR data with both numerical predictions and additional experimental measurements indicates that the 2008 LiDAR data is likely not registered properly in the longitudinal direction. A brief discussion is given in the Experimental Measurements portion of the paper above. Unless otherwise specified, no offsets have been applied to the LiDAR or QViz datasets. Some differences in the apparent agreement or disagreement between the various simulations and the measurements could be attributed to a mis-registration error.

#### NFA PREDICTIONS AND ASSESSMENTS

The objective of the numerical predictions is to assess the capability of NFA to predict unsteady transom flows of model-scale and full-scale ships.

#### *Computational Method*

The NFA code provides turnkey capabilities to model breaking waves around a ship, including both plunging and spilling breaking waves, the formation of spray, and the entrainment of air. A description of NFA and its current capabilities can be found in Dommermuth et al. (2007); O’Shea et al. (2008); and Brucker et al. (2010). NFA solves the Navier-Stokes equations utilizing a Cartesian-grid formulation. The flow in the air and water is modeled, and as a result, NFA can directly model air entrainment and the generation of droplets. The interface capturing of the free surface uses a second-order accurate, volume-of-fluid technique. A cut-cell method is

Grid Cells	Sub domains
$N_x \times N_y \times N_z$	$n_i \times n_j \times n_k$
$832 \times 384 \times 192 = 61,341,696$	$13 \times 6 \times 6 = 468$
$1664 \times 786 \times 384 = 490,733,568$	$13 \times 6 \times 6 = 468$
$2688 \times 1024 \times 384 = 1,056,964,608$	$21 \times 8 \times 6 = 1008$

Table 5 Details of NFA Numerical Simulations.

used to enforce no-flux boundary conditions on the hull. A boundary-layer model has been developed (Rottman, Brucker, Dommermuth & Broutman 2010), but it is not used in these numerical simulations, and as a result, the tangential velocities are free to slip over the hull. NFA uses an implicit sub-grid scale (SGS) model that is built into the treatment of the convective terms in the momentum equations (Brucker et al. 2010). A surface representation of the ship hull is all that is required as input in terms of hull geometry. The numerical scheme is implemented on parallel computers using Fortran 90 and Message Passing Interface (MPI). Relative to methods that use a body-fitted grid, the potential advantages of NFA’s approach are significantly simplified gridding requirements and greatly improved numerical stability due to the highly structured grid.

#### *Domain, Grids, Boundary and Simulation Conditions*

O’Shea et al. (2008) compare NFA predictions to the results of 2007 measurements. The comparisons include drag, free-surface contours in the transom region, and longitudinal wave cuts. For the 2008 comparisons, the NFA results are focused on the transom region, including mean elevations, free-surface spectral content, transverse cuts, and air entrainment. Other 2008 comparisons include predictions of drag and longitudinal wave cuts. Three grid resolutions have been performed for the 2008 data set. The highest grid resolution for the 2008 experiments uses about 45 times more grid points than the comparisons to the 2007 experiments. Most of the increased grid resolution has been concentrated in the transom region. A plane of symmetry is eliminated on the centerline, and the length of the domain has been extended by 2.5 ship lengths astern and 0.5 ship lengths ahead. NFA comparisons to the 2008 experiments show better agreement with experiments than the comparisons to the 2007 experiments that are reported in O’Shea et al. (2008) due to improvements in the theory and numerical implementation, and increased grid resolution.

NFA predictions of the free-surface elevations near a transom-stern model moving with constant forward speed are compared to laboratory measurements from the model experiment producing full-scale breaking. Table 2 provides details of the transom-stern model tests, including the length of the model, the depth of the transom, the speed of the model, and the Froude and Reynolds num-

bers.

Numerical simulations for the 7- and 8-knot cases at the 2008 trim are performed, corresponding respectively to Froude numbers  $F_r = 0.38$  and  $0.43$  and Reynolds numbers  $Re = 2.9 \times 10^7$  and  $Re = 3.3 \times 10^7$ . For 3.60 m/s (7 knots), the transom is partially wet, and for 4.12 m/s (8 knots), the transom is dry. All length and velocity scales are respectively normalized by the model’s length ( $L_o$ ) and speed ( $U_o$ ).

Table 5 provides details of the numerical simulations. The number of grid cells along the  $x$ ,  $y$ , and  $z$ -axes are respectively denoted by  $N_x$ ,  $N_y$ , and  $N_z$ . The number of sub-domains and processors along the  $x$ ,  $y$ , and  $z$ -axes are respectively denoted by  $n_i$ ,  $n_j$ , and  $n_k$ . The coarsest resolution simulation uses about 61 million grid cells, and the highest resolution simulation uses over 1 billion grid cells. The two highest grid resolutions have twice as much grid resolution along each direction as the coarsest simulation. The main difference between the two highest grid resolutions is improved grid refinement near the bow and in the lateral direction. The length, width, depth, and height of the computational domains are respectively 6.0, 1.6983, 0.66667, 0.5 ship lengths ( $L_o$ ). These dimensions match the cross section of the NSWCCD towing tank. The computational domain extends 4 ship lengths behind the transom and 1 ship length ahead of the bow. The fore perpendicular and transom are respectively located at  $x = 0$  and  $x = -1$ . The  $z$ -axis is positive up with the mean waterline located at  $z = 0$ . A plane of symmetry is not used on the centerline of the hull because small-scale turbulent structures are adversely affected.

Grid stretching is employed in all directions. Details of the grid-stretching algorithm are provided in Dommermuth, O’Shea, Wyatt, Sussman, Weymouth, Yue, Adams & Hand (2006). For the highest resolution case, the smallest grid spacing is 0.0005 near the hull and mean waterline, and the largest grid spacing is 0.01 in the far field. The numerical simulations are slowly ramped up to full speed. The period of adjustment is  $T_o = 0.5$  (Dommermuth et al. 2006). Mass conservation is ensured using the regridding algorithm that is implemented by Dommermuth et al. (2006). Density-weighted velocity smoothing is used every 400 time steps using a 3-point filter (1/4, 1/2, 1/4) (Brucker et al. 2010). The non-dimensional time step is  $\Delta t = 0.00025$ .

The simulations are run for 30,000 time steps, corresponding to 7.5 ship lengths, on the SGI® Altix® ICE (Silicon Graphics, Inc.) at the U.S. Army Engineer Research and Development Center (ERDC). The data sets are so large that only time steps 20,000 through 30,000 are saved every 40 time steps for the purposes of post processing. The 1.06 billion cell simulation takes about 90 hours of wall-clock time to run 30,000 time steps using 1008 processors. The wall-clock time can be cut in half by doubling the number of processors because NFA scales linearly. Alternatively, increasing the number of processors to over 8,000 will enable numerical simulations of breaking ship waves and tsunamis with over 10 billion grid cells within the next year.

### *Prediction Assessments*

Figure 17 compares measured wave cuts using sonic probes from the 2007 and 2008 experiments to predicted wavecuts using NFA for 3.60 m/s (7 knots) and 4.12 m/s (8 knots) speeds and four transverse locations. The NFA predictions have been time-averaged over the last 10,000 time steps for the 1.06 billion cell simulations. There is good agreement between measurements and predictions. The greatest error occurs for the cusp line wave, where NFA predictions have a lower trough than measurements. The portions of the NFA algorithm that affect the prediction of the cusp line wave are under consideration. The agreement between NFA predictions and experimental measurements in the stern region where wave breaking occurs is very good. The correlation coefficients between the predictions and the measurements average 0.95 for both 3.60 m/s and 4.12 m/s. The correlation coefficients between the 2007 and 2008 measurements average 0.97 for 3.60 m/s and 0.99 for 4.12 m/s. The RMS error between predictions and measurements average 1.0cm for 3.60 m/s and 1.6cm for 4.12 m/s. The RMS errors between 2007 and 2008 experiments are 0.86cm.

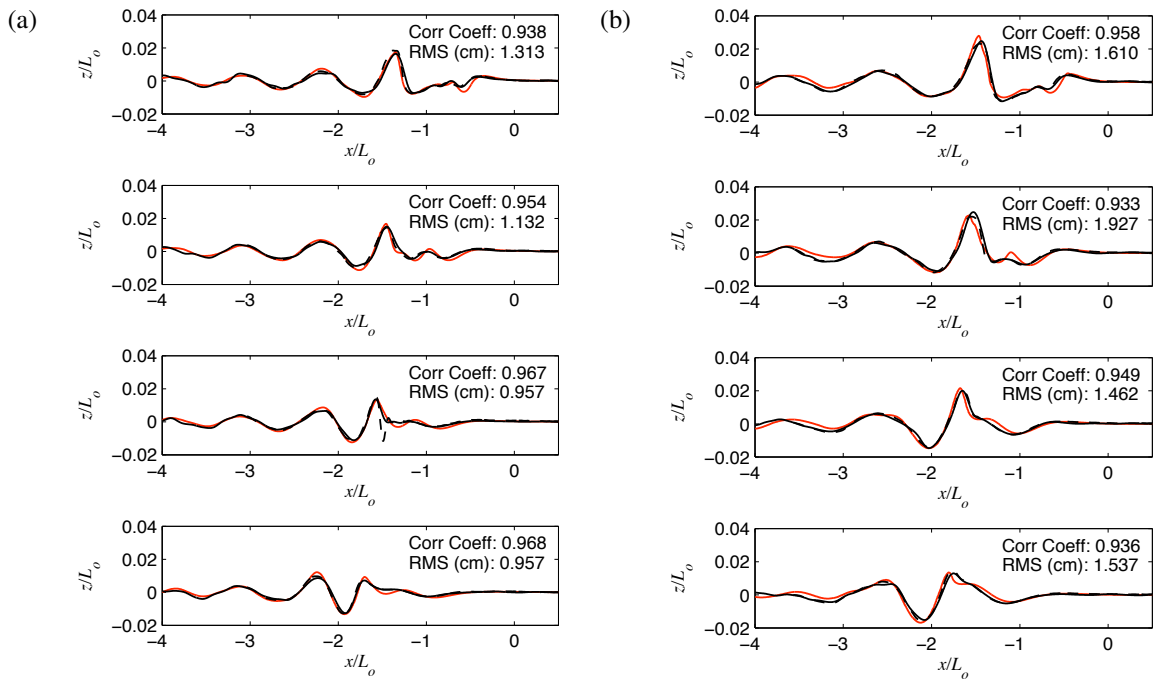
Figure 18 compares drag predictions to measurements. The viscous and wavemaking portions of the drag are calculated using the procedures outlined by O'Shea et al. (2008). The NFA results are plotted as a function of time late in the simulations to show the convergence to steady state. The numerical results have a low-frequency oscillation. As shown by Wehausen (1964), unsteady oscillations can occur in the wave resistance, and by implication the surface elevations, due to starting transients. There are also starting transients in the buildup of separation and the boundary layer on the hull, but the viscous time constants are significantly shorter than the wave resistance. The oscillations in the wave resistance occur at a period equal to  $T = 8\pi U/g$ , where  $U$  is the speed of the ship and  $g$  is the acceleration of gravity. For the 3.60 m/s (7 knots) and 4.12 m/s (8 knots) cases, the periods of oscillation are equal to 9.2 and 10.6 seconds. The time records of the drag are not long enough for

full periods of oscillation, but for the 3.60 m/s (7 knots) case, the half period of oscillation that is shown agrees with theory. The relative errors in the mean drag and RMS errors are calculated over the duration of the time record that is shown in the plot. Overall, there is very good agreement between numerical predictions and experimental measurements.

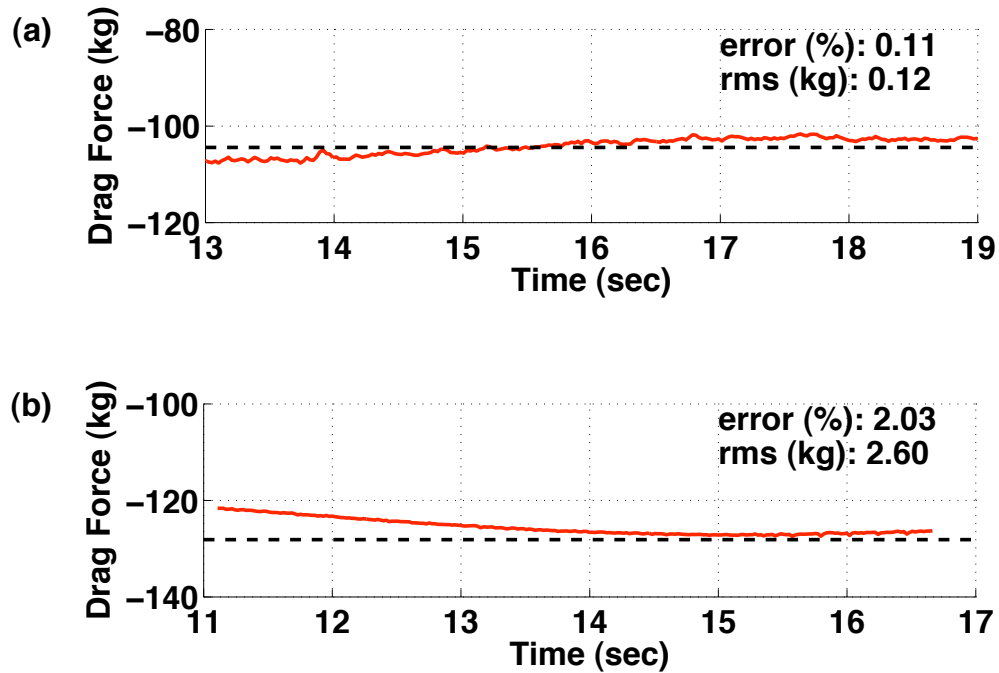
Figure 19 compares perspective views of laboratory and NFA results for 3.60 m/s (7 knots) and 4.12 m/s (8 knots). Instantaneous NFA predictions at  $t=5$  (dark blue) are overlaid time-averaged QViz measurements (light blue). The 0.5 isosurface of the volume fractions are shown for the NFA predictions. The NFA results are translucent to show the entrainment of air due to free-surface turbulence. Regions of air entrainment are denoted by a slightly darker shade of blue. The transom is partially wet for 3.60 m/s (7 knots) and fully dry for 4.12 m/s (8 knots). A glassy region is evident behind the transom at the 4.12 m/s (8 knots) speed. Significant air entrainment occurs for the 3.60 m/s (7 knot) case at the transom, in the rooster-tail region, and along the edges of the breaking stern wave. For the 4.12 m/s (8 knot) case, air entrainment first occurs on the forward face of the rooster tail and along the edges of the breaking stern wave. For both the 3.60 m/s (7 knots) and 4.12 m/s (8 knots) speeds, the measured mean profile of the free-surface elevation agrees well with instantaneous predictions. Animations of NFA results are available at <http://www.youtube.com/waveanimations>.

Figure 20 compares contours of QViz and LiDAR measurements to NFA predictions for the free-surface elevation in the transom region. Since QViz and LiDAR look down on the free surface, the NFA results are processed in a similar manner. Based on volume-fraction data, a time series of free-surface heights is calculated at particular  $x$  and  $y$  locations. The algorithm starts at the top of the domain and moves downward searching for transitions from air to water. Spray droplets of one and two grid cells are filtered out, and the highest resulting free-surface intersection is calculated. For future reference, this type of processing of the data is denoted as top-down. The correlation coefficients for Figure 20 (a) & (c), the 3.60 m/s (7 knots) and 4.12 m/s (8 knots) comparisons to LiDAR data, are respectively 0.882 and 0.905. For Figure 20 (b) & (d), the 3.60 m/s (7 knots) and 4.12 m/s (8 knots) comparisons to QViz data, the correlation coefficients are respectively 0.969 and 0.986. As discussed in the introduction, an unresolved registration issue is the likely cause of the lower correlation coefficients for the LiDAR measurements.

Figure 21 compares transverse cuts of the free-surface elevation. NFA, QViz, and LiDAR data are shown for various distances aft of the transom. In general, the agreement between NFA and QViz is excellent, whereas comparisons between NFA and LiDAR are poor.



**Figure 17:** Transom-stern model wave cuts. (a) 3.60 m/s (7 knots) and (b) 4.12 m/s (8 knots). NSWCCD measurements (2008: black lines, 2007: black dashed lines) are compared to NFA predictions (red lines). For each speed and from top to bottom, the longitudinal cuts are located at  $y/L_o=0.14375, 0.22847, 0.3125,$  and  $0.39514$ .  $x/L_o = 0$  corresponds to the bow and  $x/L_o = -1$ , the transom stern. The correlation coefficients are between NFA predictions and 2007 measurements.



**Figure 18:** Drag predictions compared to experimental measurements. (a) 3.60 m/s (7 knots) and (b) 4.12 m/s (8 knots). NSWCCD measurements (black dashed lines) are compared to NFA predictions (red solid lines).

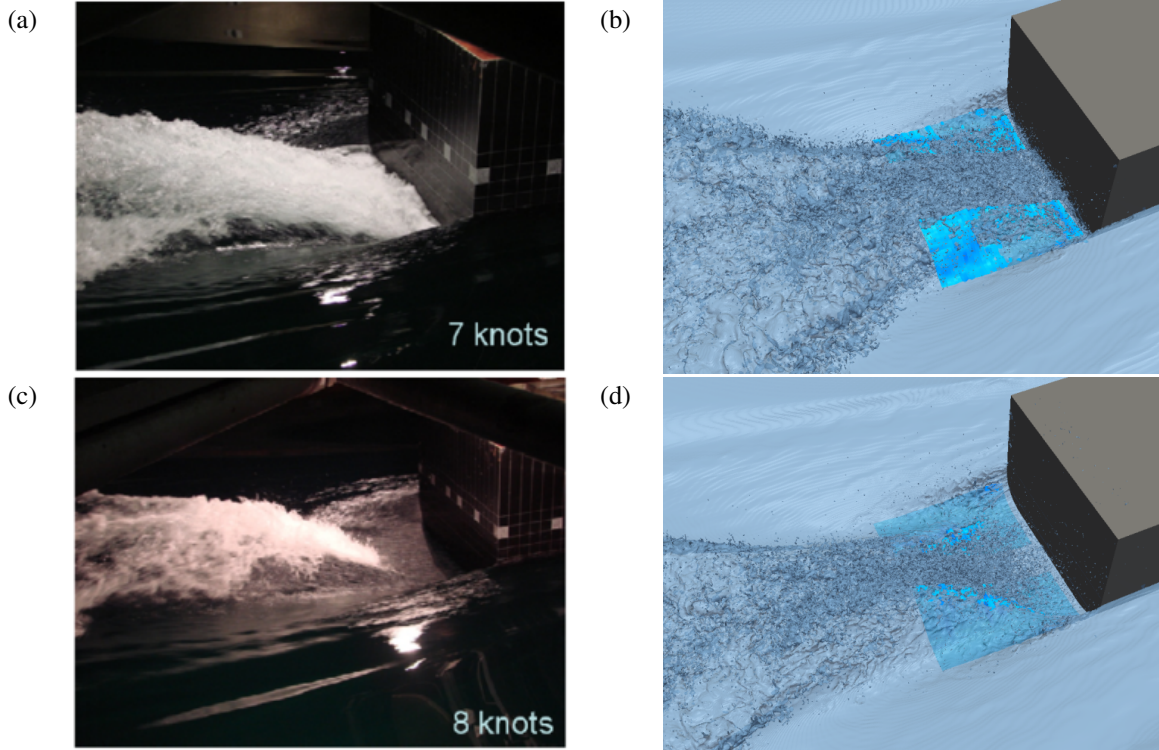


**Figure 19:** Perspective views of transom. (a) 3.60 m/s (7 knots), NSWCCD. (c) 4.12 m/s (8 knots), NSWCCD. (b) 3.60 m/s (7 knots), NFA. (d) 4.12 m/s (8 knots), NFA. The darker blue surface represents the QViz data. Both the QViz and NFA results are translucent to allow for comparison between the two results.

In the one region where all three transverse cuts overlap, NFA and QViz agree very well, but 2008 LiDAR measurements appear to be offset, see the Experimental Measurements section for a description of the offset. Aside from affecting the position of the data, the effect of improper registration upon the processing of the measurements is unknown. The LiDAR data also have some artifacts on the port side because the QViz traverse and instrumentation often prevented the LiDAR from measuring the free surface.

Figure 22 compares free-surface spectra in the transom region between measurements using QViz and LiDAR and predictions using NFA. Calculating free-surface spectra in the transom region is difficult because the position of the free surface is hard to define due to the presence of droplets, bubbles, and foam. As a complement to top-down processing, we have also developed a new processing technique that is meant to reduce noise by minimizing the influence of spray and thin sheets. We define the free surface in terms of height functions expressed in terms of the volume fraction. The calculation is performed in three steps. First, we define a height function integrating the volume fraction from the bottom of the computational domain to the top. This gives the

total amount of water in the column  $H_1$ :

$$H_1(x, y, t) = \int_{-D}^{\mathcal{H}} dz \alpha(x, y, z, t), \quad (1)$$

where  $D$  is the water depth,  $\mathcal{H}$  is the height of the domain, and  $\alpha$  is the volume fraction. Then the air pockets that are trapped beneath  $H_1$  are added back to provide a water column without bubbles.

$$H_2(x, y, t) = H_1(x, y, t) + \int_{-D}^{H_1(x, y, t)} dz (1 - \alpha(x, y, z, t)). \quad (2)$$

Finally, the droplets above  $H_2$  are subtracted out to provide a water column without bubbles and without droplets.

$$H_3(x, y, t) = H_2(x, y, t) - \int_{H_2(x, y, t)}^{\mathcal{H}} dz \alpha(x, y, z, t). \quad (3)$$

The NFA spectral analyses that are shown in Figure 22 are performed using height functions ( $H_3(x, y, t)$ ) and top-down processing. A cosine taper is applied to 5% of each end of each time series. An FFT of each time series is then applied to obtain the power spectral density plot.

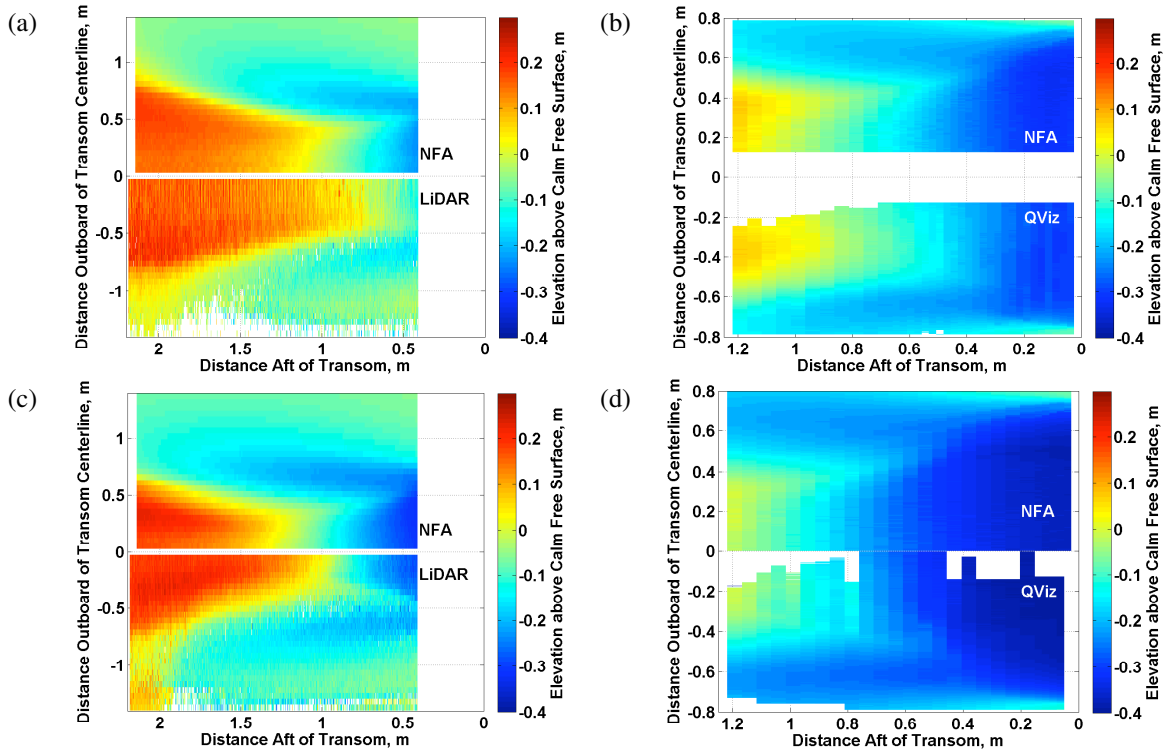


**Figure 20:** Free-surface contours. NFA predictions are above and measurements are below. (a) NFA versus LiDAR, 3.60 m/s (7 knots). (b) NFA versus QViz, 3.60 m/s (7 knots). (c) NFA versus LiDAR, 4.12 m/s (8 knots). (d) NFA versus QViz, 4.12 m/s (8 knots). All NFA results are top-down processing.

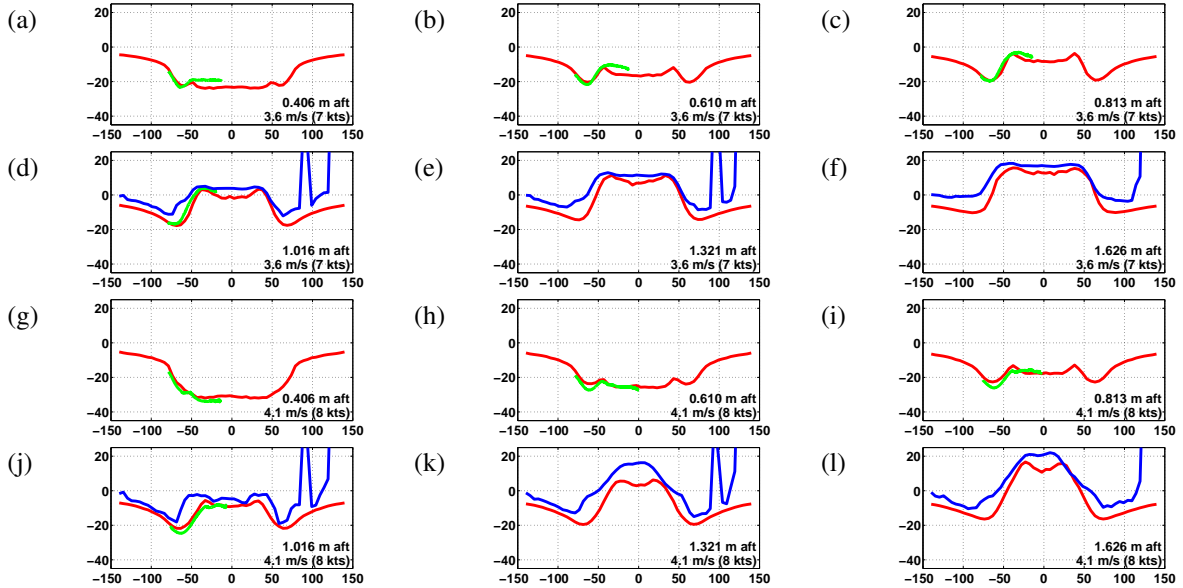


**Figure 21:** Free-surface transverse cuts.  $x$ -axis denotes distance from centerline in cm. The  $y$ -axis represents the elevation from the calm free surface in cm. Red, green, and blue lines denote NFA, QViz, and LiDAR, respectively. The large signal at  $\approx 90$  cm is due to the QViz system being within the LiDAR's field of view. See the experimental measurement section for further details. All NFA results are top-down processing.

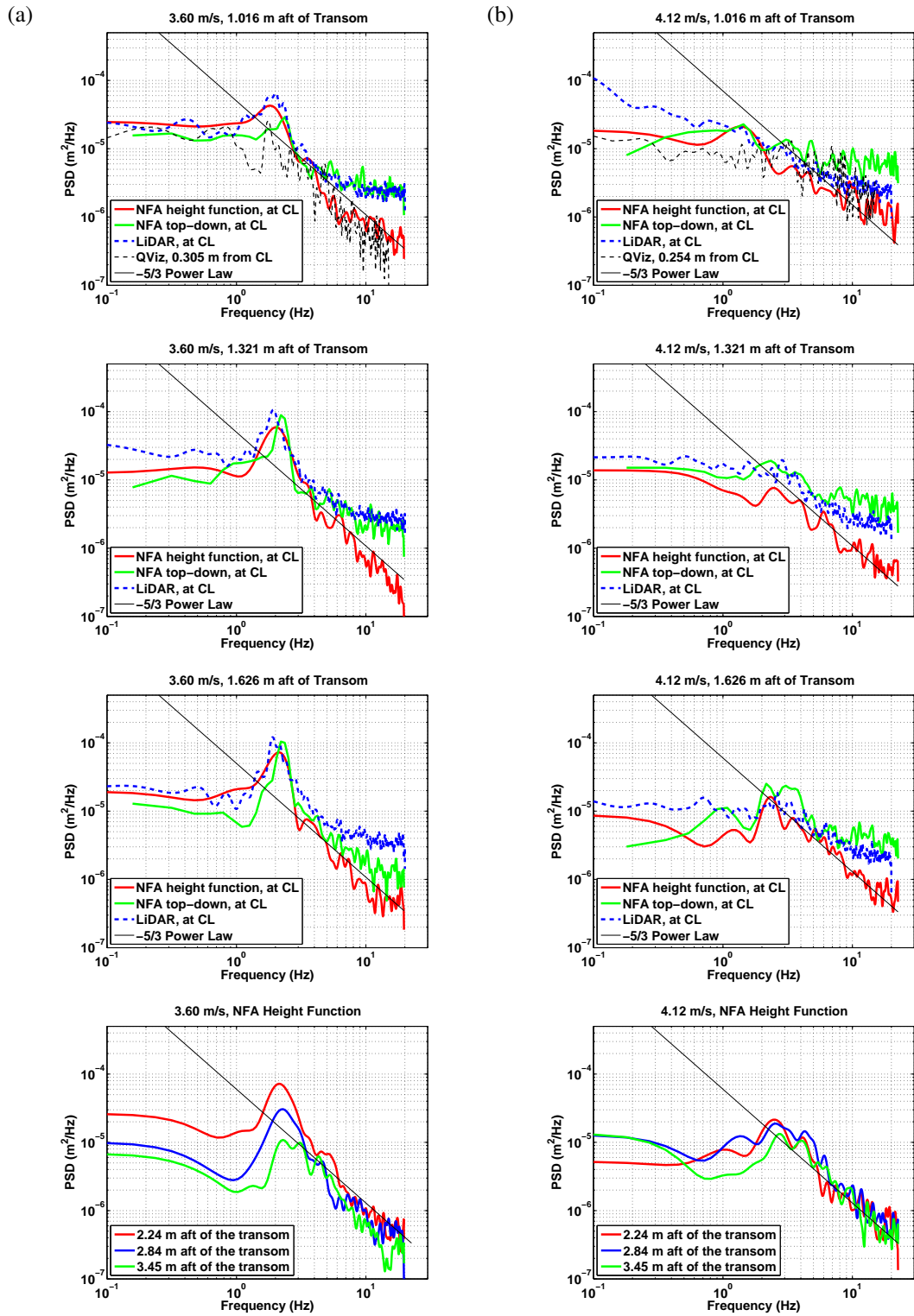
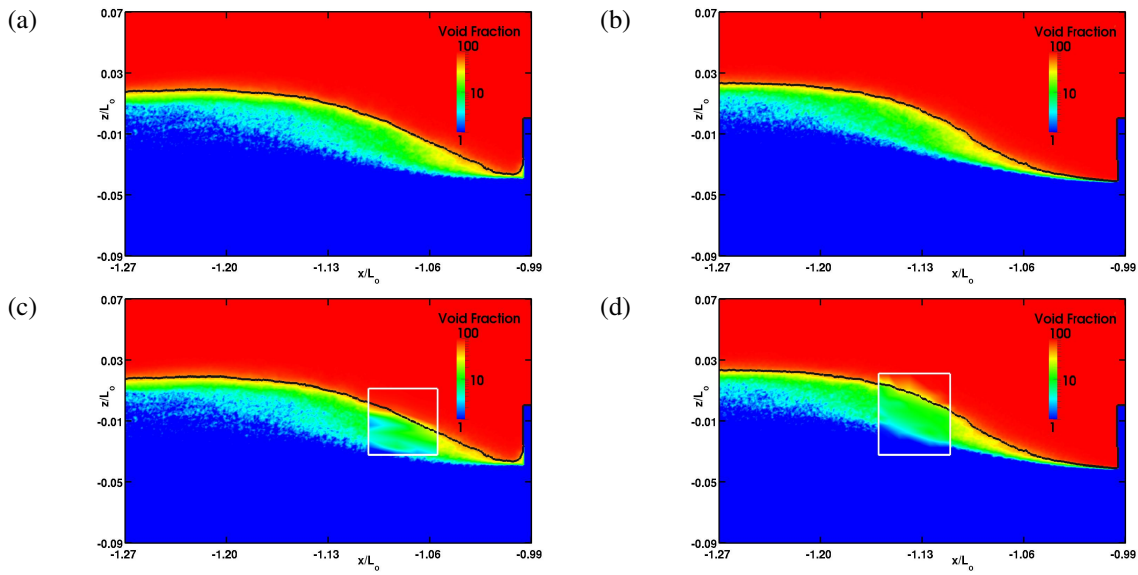


Figure 22: Free-surface spectra. NFA versus measurements. (a) 3.60 m/s (7 knots). (b) 4.12 m/s (8 knots).



**Figure 23:** Void fraction predictions compared to experimental measurements on centerplane. (a) NFA, 3.60 m/s (7 knots). (b) NFA, 4.12 m/s (8 knots). (c) NFA with void fraction measurements inserted, 3.60 m/s (7 knots). (d) NFA with void fraction measurements inserted, 4.12 m/s (8 knots). Transom is on right edge of plots. Black lines denote 0.5 isosurface. Measurements are denoted by white framing. The numerical results have been time-averaged over the last 10,000 time steps of the numerical simulation.

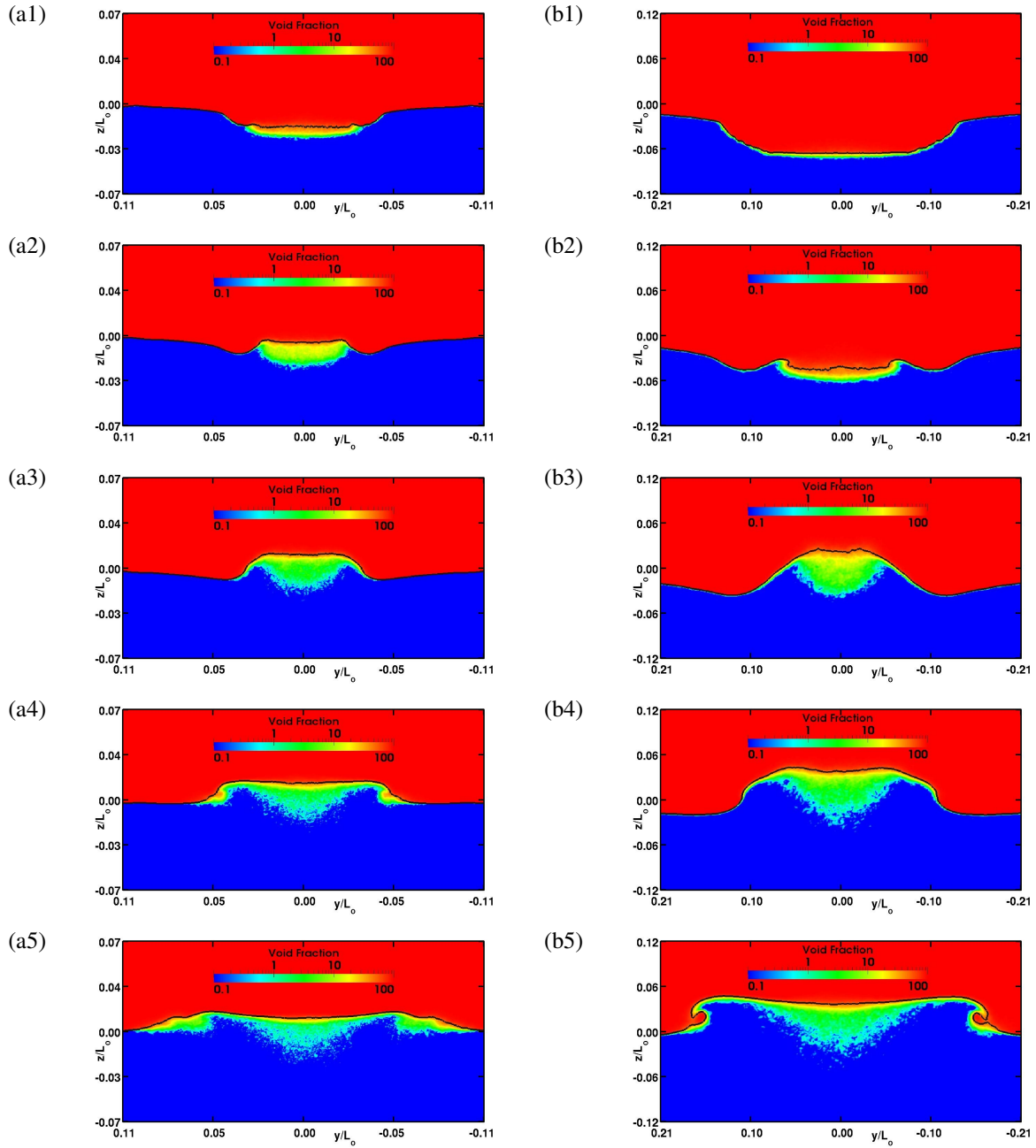
In Figure 22, top-down processing and LiDAR all have a higher noise floor than height-function processing due to the effects of spray and wave overturning. The noise floor is much lower using height-function processing. Height-function processing shows a  $-5/3$  power-law behavior for 3.60 m/s (7 knot) and 4.12 m/s (8 knot) results. QViz also shows a  $-5/3$  power-law behavior at the station closest to the transom for both speeds. There are 2 Hz features in the 3.60 m/s (7 knots) cases, and there are 2.5 Hz features in the 4.12 m/s (8 knots) cases. The 2.5 Hz features become more prominent as the distance downstream increases. The shear layer is thinner for the 4.12 m/s (8 knot) case than the 3.60 m/s (7 knot) case, which may explain why the spectral peak occurs at a higher frequency. As the distance downstream increases, the frequencies of the spectral peaks increase perhaps because the layers get thinner with less entrained air and/or the effects of turbulent decay. As a possible source of the spectral peaks, a vortex shedding mechanism off the trailing edge of the transom is not supported by the results in Figure 22 because both the 3.60 m/s (7 knot) case with a partially wet transom and the 4.12 m/s (8 knot) case with a dry transom have spectral peaks.

Figure 23 shows a centerplane cut behind the transom of NFA predictions of the void fraction compared to measurements. The top row of plots shows NFA predictions. The bottom row of plots shows NFA predictions with void-fraction measurements inserted. The plots are from 2.13m aft of the transom to the transom, and from

0.6m above the mean waterline to -0.72m below. Predictions are in good agreement with measurements. An unsteady multiphase shear layer forms in the rooster-tail region. The air is primarily entrained at toe of the spilling region and degasses over the top of the rooster tail. For the 3.60 m/s (7 knot) case, the toe moves forward and wets the transom with foam. For the 4.12 m/s (8 knot) case, the toe is slightly aft of the transom. For the 3.60 m/s (7 knot) and 4.12 m/s (8 knot) cases, the primary entrainment of air occurs aft of the transom. The shear layer is thicker and longer for the 3.60 m/s (7 knot) case than for the 4.12 m/s (8 knot) case. The difference in thicknesses and amount of air entrainment affects the temporal and spatial structure of the shear layer, which is evident in the spectra in Figure 22. The foam that wets the transom in the 3.60 m/s (7 knot) case does not appear to have enough momentum to affect the drag of the ship. At present, there is no evidence of large-scale vortical structures being shed from the transom in the NFA simulations. If coherent structures are being shed from the backside of the transom, they must be dynamically weak due to the entrained air. The results of the NFA simulations suggest that the spatial and temporal structure that is observed in the rooster-tail region for 3.60 m/s (7 knot) and for 4.12 m/s (8 knot) at shorter scales and higher frequencies is due to the effects of unsteady multiphase shear layers.

Figure 24 shows transverse cuts of the time-averaged volume fraction for various distances aft of the





**Figure 24:** Air entrainment due to wave breaking. Color contours of the time-averaged volume fraction are plotted for various transverse cuts. The black lines denote the 0.5 isosurface of the volume fraction. (a) 3.60 m/s (7 knots) and (b) 4.12 m/s (8 knots). (1)  $x/L_o = 0.04$ , (2)  $x/L_o = 0.08$ , (3)  $x/L_o = 0.16$ , (4)  $x/L_o = 0.24$ , (5)  $x/L = 0.32$ . Here,  $x$  and  $L_o$  are respectively the distance aft of the transom and the length of the model. The numerical results have been time-averaged over the last 10,000 time steps of the numerical simulation.

transom. The 3.60 m/s (7 knot) plots extend from -1m to 1m in transverse direction and from -.62m to .64m in the vertical. The 4.12 m/s (8 knot) plots extend from -1.9m to 1.9m in transverse direction and from -1.14m to 1.14m in the vertical. Most of the air entrainment occurs in the rooster-tail region and along the edges of the stern breaking wave. The structure of the void fraction wake has three dominant structures corresponding to the centerline entrainment in the rooster-tail region and the spilling-breaking entrainment that occurs along the cusp line.

## CFDShip-IOWA PREDICTIONS AND ASSESSMENTS

CFDShip-Iowa V4 mean and unsteady wave elevation predictions using detached eddy simulation (DES) for the transom stern model for a wet ( $F_r = 0.38$ ) and a dry ( $F_r = 0.43$ ) transom is assessed using experimental data, and the dominant wetted transom flow frequency is explained as a Karman-like vortex shedding.

### Computational Method

The simulations are performed using a single phase solver in absolute inertial earth-fixed coordinates (Carrica, Wilson & Stern 2007). The turbulence modeling is performed using DES and the interface modeling using level-set methods. A multi-block overset grid approach is used to allow grid refinement in the regions of interest. The governing equations are discretized using cell-centered finite difference schemes on body-fitted curvilinear grids and solved using a predictor-corrector method. The time marching is done using the  $2^{nd}$  order backward difference scheme. The convection terms and level-set equations are discretized using a hybrid  $2^{nd}/4^{th}$  order Total Variation Diminishing (TVD) scheme. The pressure Poisson equation is solved using the Portable Extensible Toolkit for Scientific computing (PETSc) using a projection algorithm to satisfy continuity. MPI-based domain decomposition is used, where each decomposed block is mapped to a single processor.

### Domain, Grids, Boundary and Simulation Conditions

The simulations are performed for half of a domain only as shown in Figure 25. The grid consists of a background block  $X/L_o = [-0.5, 3.0]$ ,  $Y/L_o = [0, 1.0]$ , and  $Z/L_o = [-1.0, 0.035]$ , where  $X$ ,  $Y$ ,  $Z$  and  $L_o$  are the streamwise, spanwise, normal directions and ship length, respectively. Refinement blocks are used near the free-surface and in the transom region to accurately resolve the transom flow features. The grid consists of a total of 16.5M points, which is partitioned into 98 blocks for parallel computing. The uniform inlet velocity  $U$ , zero-gradient exit, far-field at  $Z$ -Min,  $Z$ -Max and  $Y$ -Max planes, and  $Y = 0$  symmetric boundary conditions

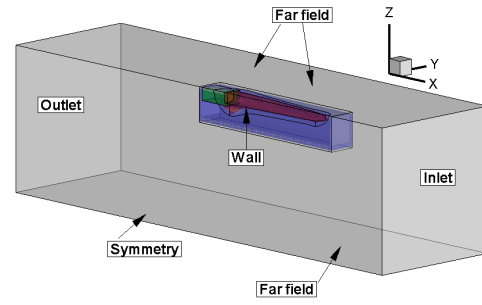


**Figure 25:** Domain and boundary conditions for CFDShip-Iowa V4.

are applied to the background grid. The no-slip boundary condition is applied at the boundary layer grid  $J=1$  plane. The averaged  $y^+ = 0.8$  to  $1.0$  for the near-wall resolution. The boundary layer grid is translated and rotated to match the sinkage and trim from the experimental test.

Fixed sinkage and trim simulations are performed for the speeds of 3.60 m/s (7 knots) ( $Re = 1.093 \times 10^7$ ,  $F_r = 0.3803$ ) and 4.12 m/s (8 knots) ( $Re = 1.25 \times 10^7$ ,  $F_r = 0.4346$ ). The  $Re$  values are computed assuming  $20^\circ$  C water temperature. Simulations are performed using a time step size  $\Delta t = 2.5 \times 10^{-3}$ . The 3.60 m/s (7 knots) simulation is performed for a time equivalent to 8.5 ship lengths ( $8.5L_o/U$ ), and every fourth time-step solution for the last  $6L_o/U$  data is used for averaging. The 4.12 m/s (8 knots) simulation is performed for only  $6.5L_o/U$  as flow reaches a steady state sooner and averaging is performed for the last  $2L_o/U$  data.

### Prediction Assessments

The wave elevation mean, RMS, and elevation spectra results were compared against QViz close to the transom and LiDAR away from the transom. Void fraction data are not compared, as they cannot be quantified by the level-set interface modeling.

The validation study focuses only on the comparison error  $E$  between the experimental and CFDShip-Iowa V4 results, as a grid verification study was not performed. Thus the grid uncertainty  $U_G$  or validation uncertainty intervals cannot be estimated.  $U_I = 0.7\%$  based on the resistance prediction  $C_t$  are similar to that predicted for the CFDShip-Iowa V4 appended Athena study (Bhushan, Xing & Stern 2010). As shown in Figure 26, the resolved turbulent kinetic energy (TKE) levels are greater than 92% of the total TKE (modeled + resolved) in the transom stern region for both flow conditions. This result suggests that the grid is sufficiently fine to properly resolve the turbulent fluctuation in the Large Eddy Simulation (LES) region. Herein, only half domain simulations are performed, which may result in under prediction of RMS as observed by Bhushan et al. (2010).

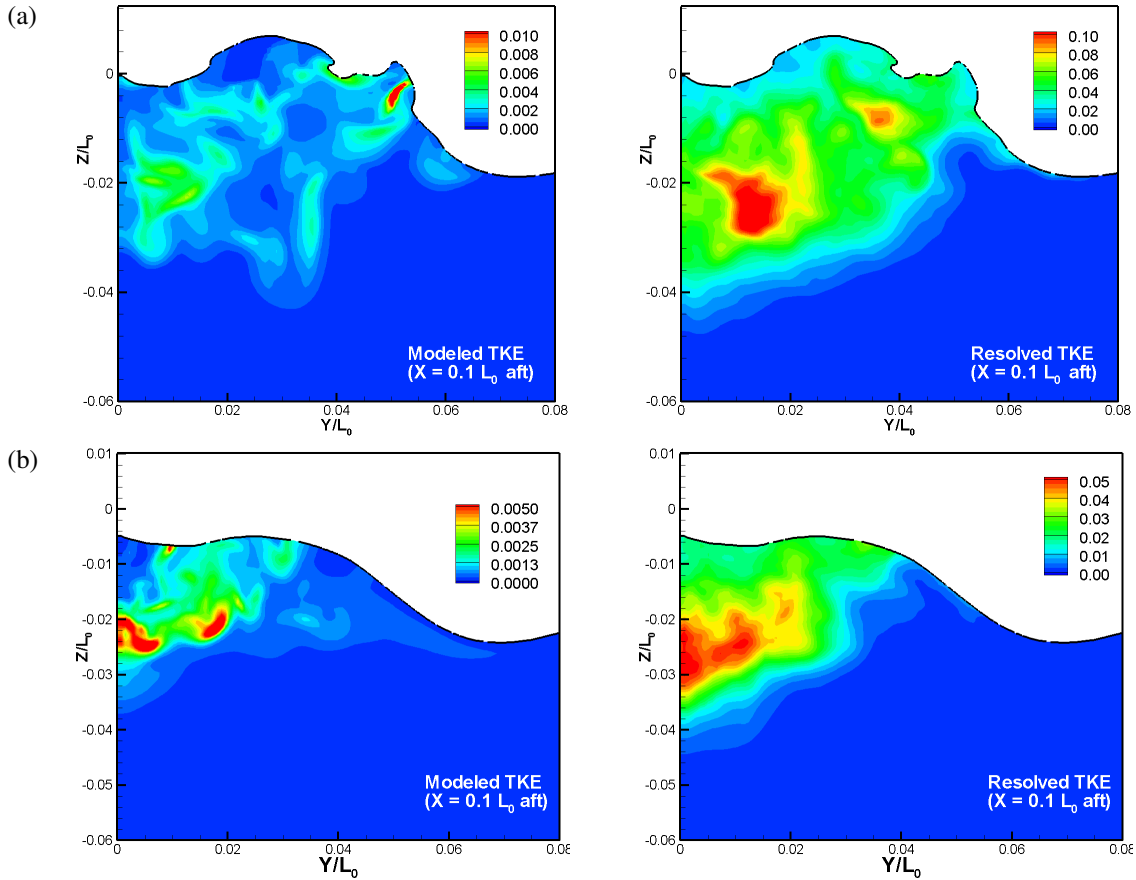


**Figure 26:** Modeled (left) and resolved (right) TKE predictions using CFDSHIP-Iowa V4 for (a) 3.60 m/s (7 knots), and (b) 4.12 m/s (8 knots) simulations at  $X/L_o = -1.1$ .

An unsteady  $C_t$  is predicted for 3.60 m/s (7 knots), whereas steady values are predicted for 4.12 m/s (8 knots) as shown in Figure 27. The time period of the  $C_t$  unsteadiness,  $\tau_p = 0.21L_o/U$ , is due to the transom vortex shedding and will be discussed later. As summarized in Table 6, the total drag predictions are 4.18% and 2.61% higher than the experimental results for 3.60 m/s (7 knots) and 4.12 m/s (8 knots), respectively.

The experimental results show a wetted transom flow for the 3.60 m/s (7 knots) case with a recirculation region on either side of the model centerline. As shown in Figure 28, the wake spans the entire transom width and is dominated by a large amount of entrained air. For the 4.12 m/s (8 knots) case, a dry transom was observed with a rooster tail which begins to form at  $X/L_o = 0.07-0.1$  aft of the transom. The wake in this case is well defined, narrow, and quickly steepens to a defined peak where it begins to spill out and widen. CFDSHIP-Iowa V4 predicts a wetted transom for 3.60 m/s (7 knots) with unsteady vortex shedding from the transom bottom corner. Wave breaking and air entrainment is predicted up to the tran-

som edge. For the 4.12 m/s (8 knots) case, a rooster tail begins to form at  $X/L_o = 0.086$  aft of the transom, a narrow wake is observed up to  $X/L_o = 0.15$  aft, and starts to widen thereafter. The breaking wave and air entrainment occurs mostly in the rooster tail region.

The experimentally measured mean wave elevation in Figure 29 shows good agreement between the QViz and LiDAR datasets in the small overlap region for both 3.60 m/s (7 knots) and 4.12 m/s (8 knots). The datasets show a low wave elevation near the transom and a diverging wave trough emerging from the transom edge. The diverging wave angle is  $20.2^\circ$  and  $26^\circ$  at 3.60 m/s (7 knots) and 4.12 m/s (8 knots), respectively. A transverse wave is observed between the centerline and the diverging wave at both speeds, with the wave forming further back at a speed of 4.12 m/s (8 knots) than the 3.60 m/s (7 knot) case.

CFDSHIP-Iowa V4 predictions are within 3-4% of the experimental results both near the transom and in the diverging waves trough at 3.60 m/s (7 knots) and 4.12 m/s (8 knots). The diverging wave peak is predicted to be

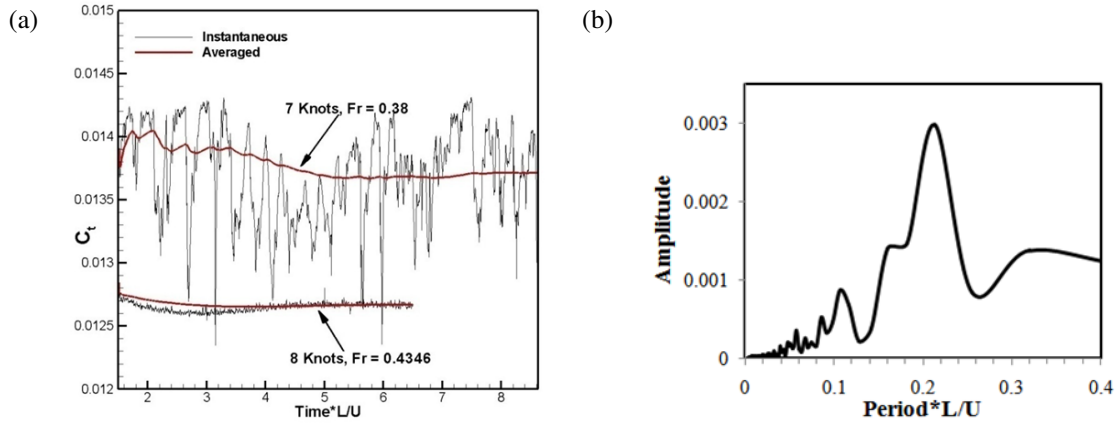


Figure 27: CFDShip-Iowa V4  $C_t$  prediction (a) time history, and (b) spectra for 3.60 m/s (7 knots).

Table 6 Resistance, mean and unsteady wave elevation validation for transom-stern model, and bare hull and appended Athena

Geometry	Flow Conditions			$C_t$	Drag* (lb)	Mean wave elevation	Wave elevation RMS	Dominant Frequency (Hz)
Transom-stern model	$Re = 1.09 \times 10^7$ , $Fr = 0.38$	EFD	$D$	-	230.24	Fig. 4	Fig. 5	1.96
		2008 NSWCCD test	$U_D \% D$	-	1.06			
		CFDShip-Iowa V4	$S$	$1.371 \times 10^{-2}$	239.87	Fig. 4	Fig. 5	1.9
			$U_I \% S$			0.7		
			$E \% D$	-	+4.18	4.5	-	0.1%
Transom-stern model	$Re = 1.25 \times 10^7$ , $Fr = 0.4346$	EFD	$D$	-	282.47	Fig. 10	Fig. 11	None (Fig. 8)
		2008 NSWCCD test	$U_D \% D$	-	0.5			
		CFDShip-Iowa V4	$S$	$1.265 \times 10^{-2}$	289.86	Fig. 10	Fig. 11	None (Fig. 8)
			$U_I \% S$			0.7		
			$E \% D$	-	+2.61	6.5	-	-
Fully Appended Athena	$Re = 2.9 \times 10^8$ , $Fr = 0.25$	EFD	$D$	$5.732 \times 10^{-3*}$				0.95
		Wyatt et al. (2008)	$U_D \% D$	-		7.63		
		CFDShip-Iowa V4 Bhushan et al. (2010)	$S$	$5.49 \times 10^{-3}$				0.9
			$U_{3\%} \% S$	6.36		17.47	13.23	9.8
			$E \% D$	4.22		10-12	8-10	5.6
$U_I \% D$	-			19.06	15.27	12.42		
Athena bare hull	$Re = 1.98 \times 10^7$ , $Fr = 0.43$	EFD	$D$	$5.53 \times 10^{-3}$				
		Fu et al. (2005)	$U_D \% D$	-		-		
		CFDShip-Iowa V4 Wilson et al. (2006)	$S$	$5.49 \times 10^{-3}$				
			$U_I \% S$	0.29		-		
			$E \% D$	0.66		4.3		

\*Computed assuming water temperature of 20°C.

†Extrapolated from model-scale using ITTC correlation line.

- : Results not available or cannot be computed.

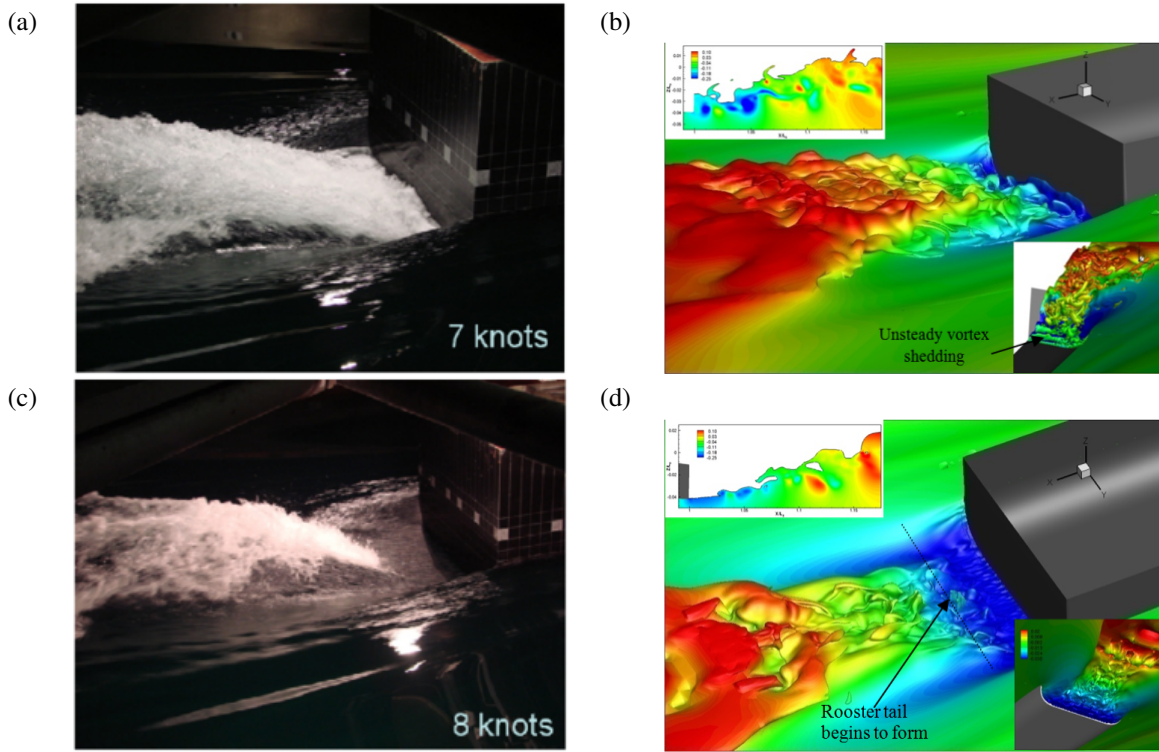


**Figure 28:** Images of the instantaneous transom wave elevation during NSWCCD testing (left panel) and CFDSHIP-IOWA V4 (right panel) for (a,b) 3.60 m/s (7 knots),  $F_r = 0.38$ , and (c,d) 4.12 m/s (8 knots),  $F_r = 0.43$ . Inset shows wave elevation at  $Y/L_o = 0.01$  colored using piezometric pressure, and wave elevation and isosurface of  $Q$ -criterion = 3000 (Hunt et al. 1988) as viewed from the bottom

outside the LiDAR’s measurement window and thus will not be compared. The diverging wave angle is 12% and 10% higher than that found during the NSWCCD testing for 3.60 m/s (7 knots) and 4.12 m/s (8 knot), respectively.

A shoulder wave is seen in the wake elevation cross-sections for both the 3.60 m/s (7-knot) and 4.12 m/s (8-knot) cases. There are slight indications of a shoulder wave in the LiDAR results, likely due to the large RMS at those locations and the uncertainty inherent in the LiDAR measurements ( $\pm 2.54$  cm). CFDSHIP-IOWA V4 transverse wave peak elevation predictions are within 2-4% of the experimental results for both the 3.60 m/s (7 knot) and 4.12 m/s (8 knot) cases for the location closest to the transom. At 4.12 m/s (8 knots) the peak values reported by CFDSHIP-IOWA V4 are lower by 25% for the locations further from the transom. For the farthest cross section, almost uniform elevations are observed in the wake at 3.60 m/s (7 knots), which agrees within 2% of the experimental results.

Both LiDAR and CFDSHIP-IOWA V4 indicate high RMS values in the transverse wave region with a peak at the centerline at both 3.60 m/s (7 knots) and 4.12 m/s (8 knots). Values taper off outside the wake region due to

breaking as shown in Figure 30(b).

CFDSHIP-IOWA V4 mean wave cut predictions in Figure 31(a) compare within 4-5% of the experiments for the first three locations at a speed of 3.60 m/s (7 knots). An averaged error of 7-9% is obtained for the farthest transverse wave cut locations. At 4.12 m/s (8 knots) the two closest transverse wave cut locations agree within 2-4% of the experimental results. For the two outer locations, the peak values are 20-30% lower than the experimental data. A lag is expected between the CFDSHIP-IOWA V4 and experimental results due to the differences in the diverging wave angles for both model speeds.

The wave elevation spectra from the LiDAR measurements in Figure 32(a) show a dominant frequency of 1.96Hz at all the locations at a speed of 3.60 m/s (7 knots). CFDSHIP-IOWA V4 predicts the dominant frequency within 0.1% of the experiments, but the peak amplitude is under predicted by 10%. CFDSHIP-IOWA V4 results show large amplitude oscillations for high frequencies, which could be due to the iterative error in the level-set function. At a speed of 4.12 m/s (8 knots), the results between CFDSHIP-IOWA V4 and the experimental results agree well. No spectral peak is seen at this speed.

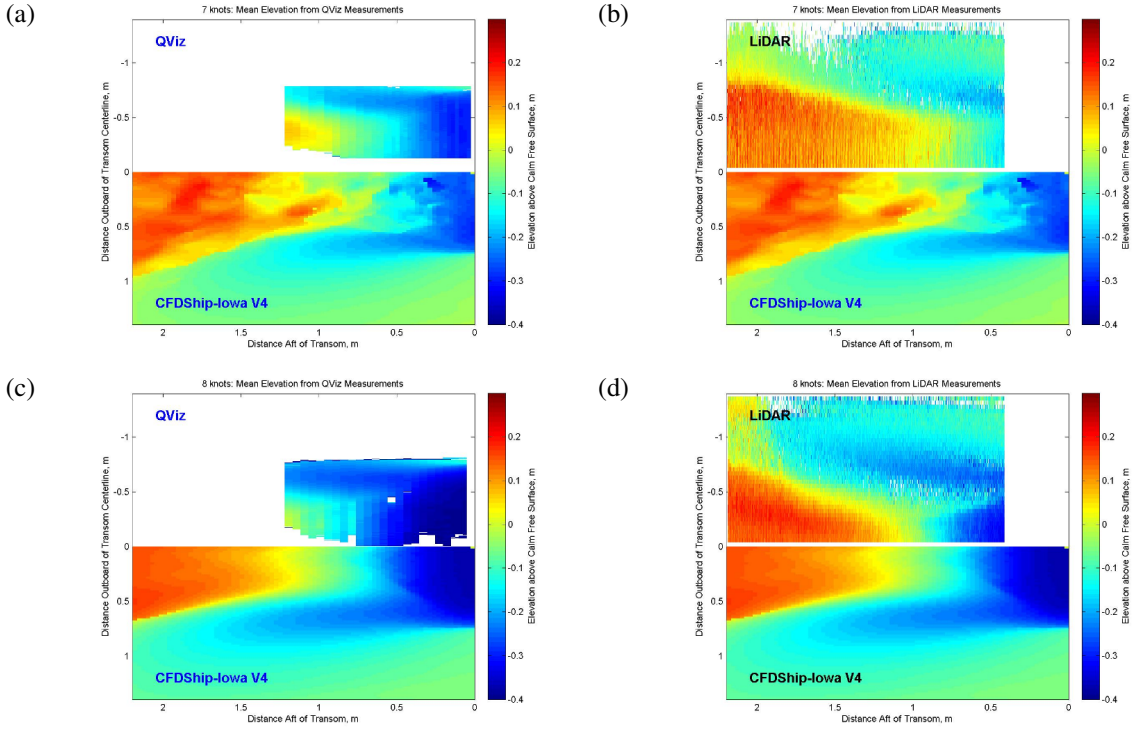


**Figure 29:** CFDSHIP-IOWA V4 (top) mean transom wave elevation predictions for 3.60 m/s (7 knots) are compared with (a) QViz, (b) LiDAR measurements (top), and for 4.12 m/s (8 knots) (c) QViz, and (d) LiDAR measurements. The transom edge is at  $X/L_o = 1.0$ .

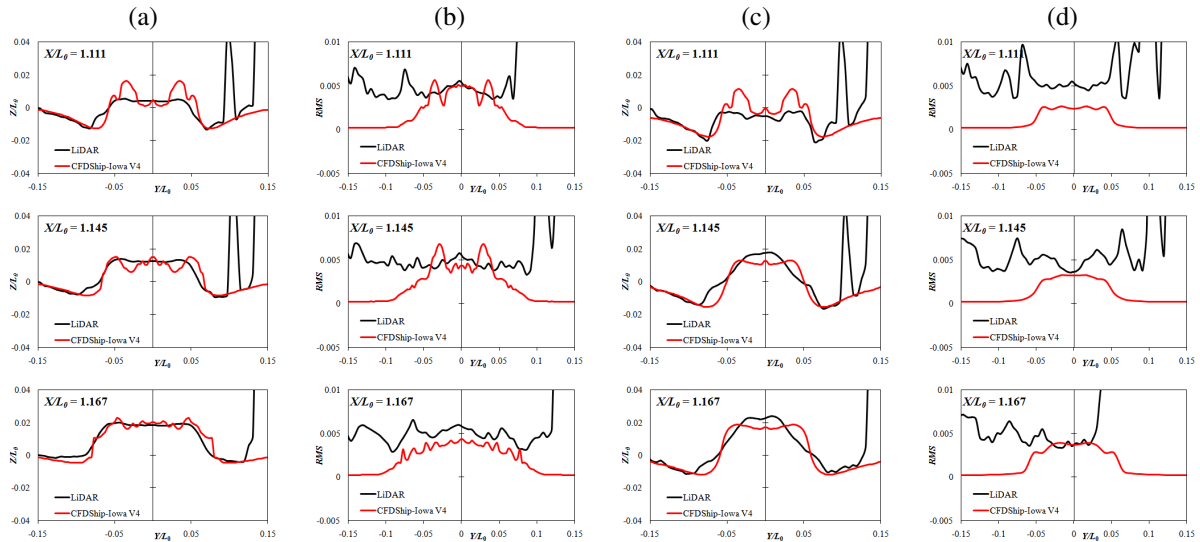


**Figure 30:** Free-surface transverse cuts.  $x$ -axis denotes distance from centerline in cm. The  $y$ -axis represents the elevation from the calm free-surface in cm. Red, black lines denote CFDSHIP-IOWA V4 and LiDAR results, respectively. Column (a) 3.60 m/s (7 knots), mean height 0.254m, 0.508m aft and 0.762m aft. Column (b) 3.60 m/s (7 knots), RMS 0.254m, 0.508m aft and 0.762m aft. Column (c) 4.12 m/s (8 knots), mean height 0.254m, 0.508m aft and 0.762m aft. Column (d) 4.12 m/s (8 knots), RMS 0.254m, 0.508m aft and 0.762m aft.

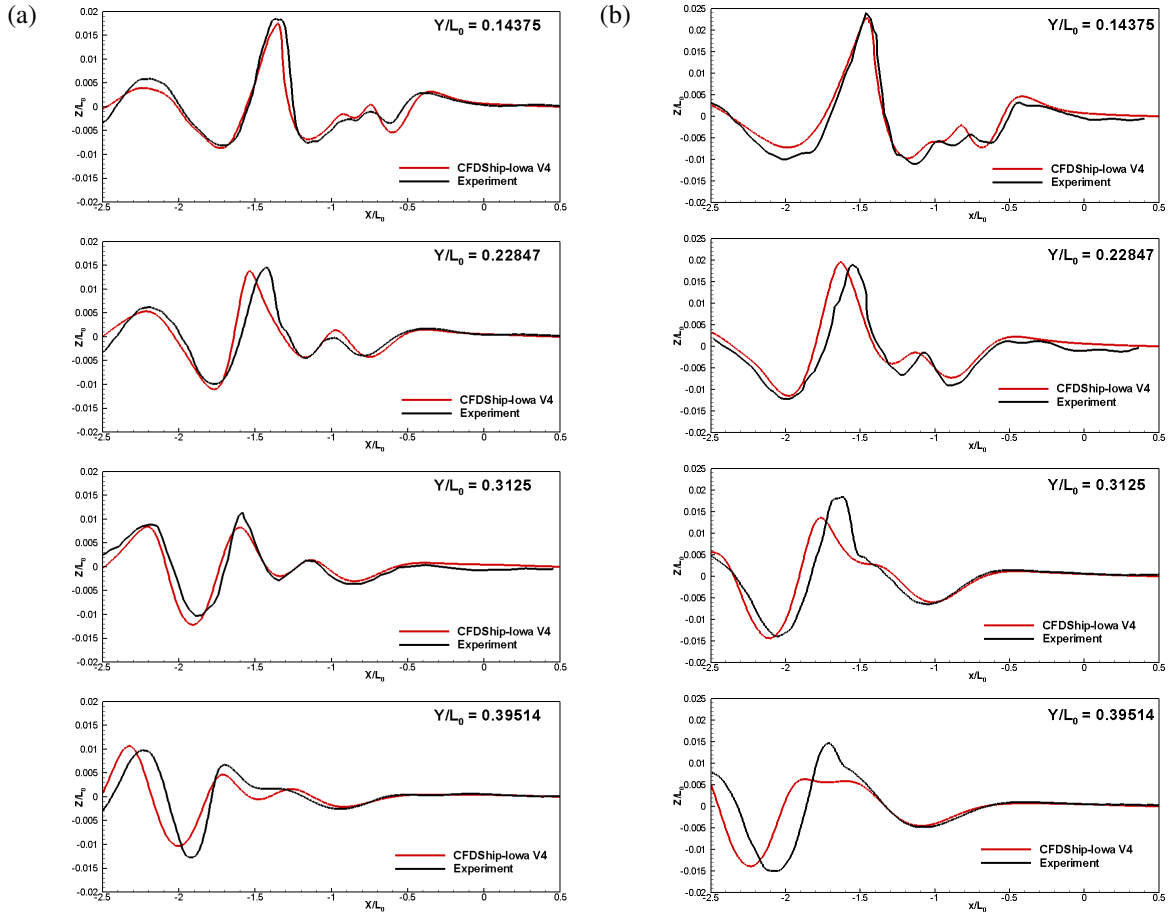


**Figure 31:** Transom-stern model wave cuts at  $Y/L_o = 0.14375, 0.22847, 0.3125$  and  $0.39514$  predicted by CFDShip-Iowa V4 is compared with Senix Ultrasonic Sensors measurements for (a) 3.60 m/s (7 knots) and (b) 4.12 m/s (8 knots). The X coordinates are oriented to match the experiment's coordinates, i.e.,  $X = 0$  corresponds to bow and  $X = -1$  the transom stern.

**Table 7** Characteristics of the Karman-like vortex shedding for different geometries

Geometry, Flow and Simulation Condition	Velocity Scale, $U$	Length Scale		Frequency		$St_H = fH/U$
		Evaluation Method	$H$	Evaluation Method	$f$	
Different geometries with and without free-surface (Kandasamy et al., 2008)	Shear velocity	Half wake width	-	-	-	0.066-0.069
Bare hull Athena, $Fr = 0.25$ , model-scale URANS (Wilson et al., 2006)	Free-stream velocity	Wetted transom height	0.007	$C_t$	12.58	0.088
Bare hull Athena, $Fr = 0.25$ , model-scale DES (Bhushan et al., 2010)			0.008	$C_t$	18.55	0.148
Appended Athena, $Fr = 0.25$ , model- and full-scale DES (Bhushan et al., 2010)			0.0125 - 0.0128	Piezometric pressure at transom corner	8.3	0.098 - 0.107
Transom-stern model, $Fr = 0.38$ , model-scale DES			0.015	$C_t$ and wetted hull area	5	0.075

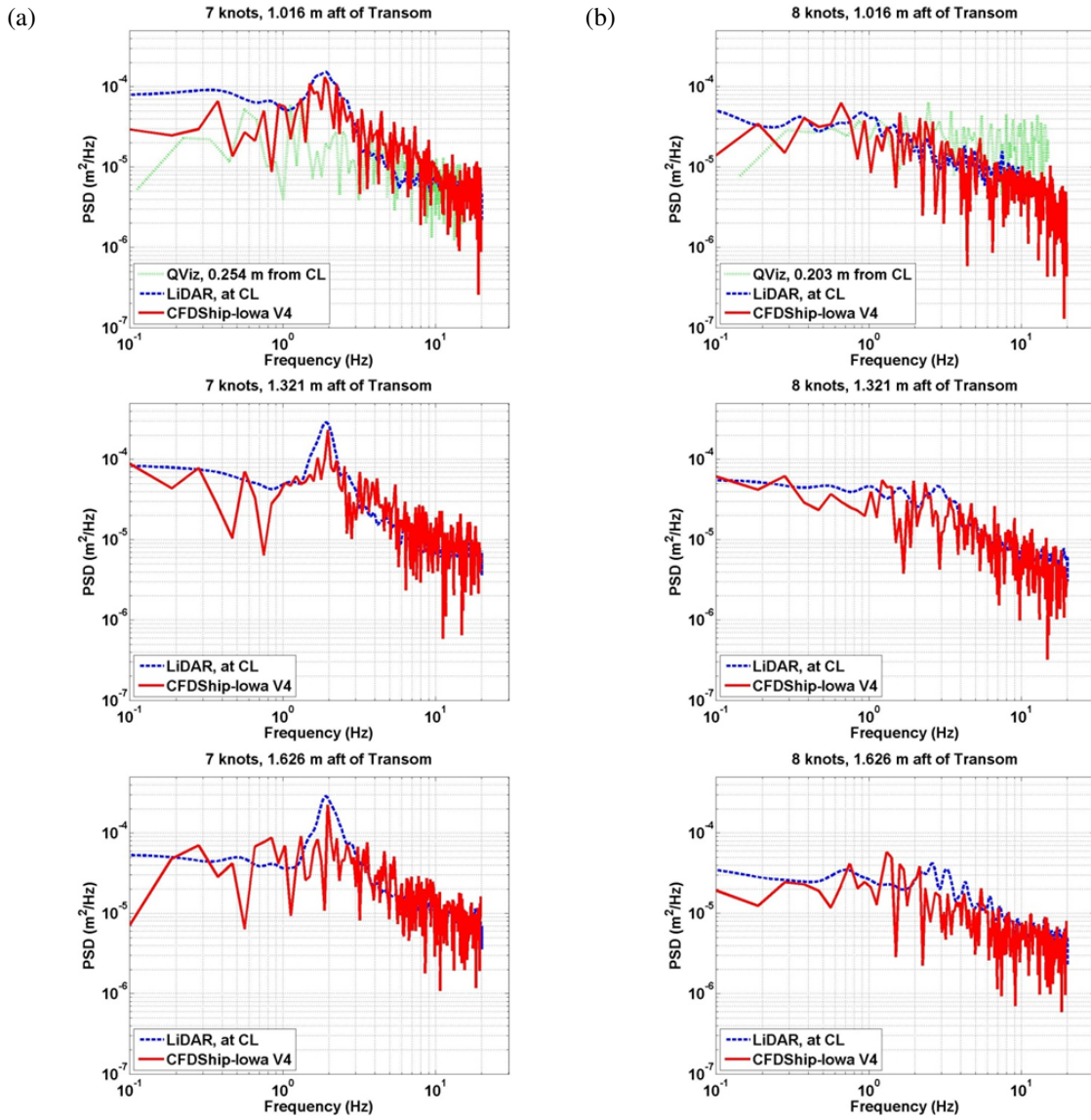


**Figure 32:** Spectra of wave elevation unsteadiness at  $X/L_o = 1.016, 1.321$  and  $1.626$  predicted by CFDSHIP-IOWA V4 is compared with experimental data for (a)  $3.60$  m/s (7 knots) (a)  $3.60$  m/s (7 knots) and (b)  $4.12$  m/s (8 knots).



The flow streamlines exit parallel to the hull bottom for this case, and vortical structures are not predicted near the transom region. Any remaining unsteadiness is likely due to wave breaking.

Overall, the experimental datasets are reasonably good for the drag, mean wave elevation and wave-cuts. RMS datasets do not show any coherent pattern, but the spectra do show a dominant frequency at 3.60 m/s (7 knots) and the dominant frequency compares within 0.1% of the experiments. CFDSHIP-Iowa V4 drag predictions are 4.18% higher than the experimental measurements at 3.60 m/s (7 knots) and 2.61% higher at 4.12 m/s (8 knots). CFDSHIP-Iowa V4 predictions show a peak in the transom wave elevation cross-section close to the transom in the shoulder region, which was not observed in the LiDAR data. The mean wave elevation and wave-cut predictions are 4% higher when compared to the experimental results at 3.60 m/s (7 knots) and 7% higher at 4.12 m/s (8 knots). The limited validation here supports the credibility of CFDSHIP-Iowa V4 simulation results.

The transom vortex shedding is analyzed from the volume solution as shown in Figure 33. The wave elevation at the transom increases when the vortex forms at the transom corner and decreases as the vortex is shed, whereas the wave elevation elsewhere on the hull remains the same. This mechanism induces an unsteady hull-wetted area with a frequency that is the same as that of transom vortex shedding. Similarly, the  $C_t$  decreases as the transom wave elevation increases due to the excess pressure acting on the transom, and vice versa. Thus either  $C_t$  or hull-wetted area can be used to evaluate transom vortex shedding frequency, and the former was previously used for the bare hull Athena study (Wilson, Carrica & Stern 2006). As expected, both hull-wetted area and  $C_t$  give the same  $\tau_p = 0.21L_o/U$ , i.e., frequency = 1.9Hz, which is confirmed from the volume solution analysis. The transom vortex shedding frequency is within 3% of the transom wave elevation unsteadiness, thus is identified to be the main cause of transom wave elevation unsteadiness. Similar results were obtained for the bare hull and appended Athena wetted transom flow.

The transom vortex shedding is identified as the Karman-like shedding as in the Athena studies. As summarized in Table 7, transom-model  $\tau_p$  is 70% and 36% higher than those predicted for bare hull and appended Athena using CFDSHIP-Iowa V4 DES at  $F_r = 0.25$ , respectively. The averaged wetted transom height  $H = 0.0145$  is 51% and 13% higher than the values predicted for bare hull and appended Athena studies, respectively. This gives  $St_H = fH/U = 0.075$ , which is half of that predicted for bare hull and 33% lower than that for appended Athena.  $St_H$  is 8.5% higher than the upper limit of the Karman-like shedding  $St_H$  range of 0.066-0.069 (Kandasamy, Xing & Stern 2008) for different geome-

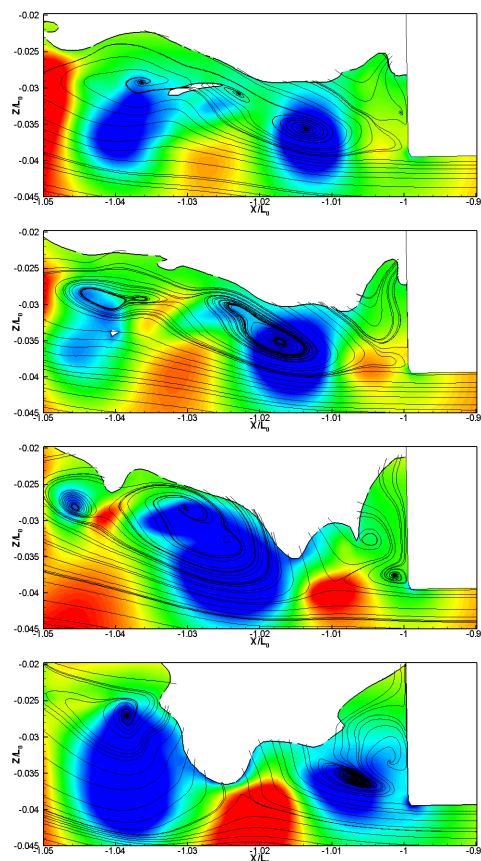


**Figure 33:** Analysis of unsteady transom vortex shedding predicted by CFDSHIP-Iowa V4 for 3.60 m/s (7 knots). (a) Quarter phases of transom vortex shedding are shown by streamlines and contours of piezometric pressure at  $Y/L_o = 0.01$  plane.

tries with and without a free-surface.

## CONCLUSIONS

### *Experimental Measurements*

We have presented a summary of data obtained from a series of experiments on a model transom stern. The aim of the experimental work was to obtain an understanding of the gross transom wake properties as well as detailed statistical measurements across the wet/dry transom condition. A variety of instrumentation was used and there is generally good agreement between the results, despite an uncertainty in the registration of the LiDAR.

The experimental work described in this paper demonstrates the utility of such measurements compared to larger-scale field experiments. While full-scale experiments allow for in-situ measurements of the transom stern wake, accurate and repeatable measurements in the

field are difficult to make. Laboratory experiments allow for more detailed measurements on specific aspects of the flow that would not be possible in the field. The ability to obtain highly repeatable wake elevation measurements from instruments such as the LiDAR are essential to our understanding of the full-scale breaking transom wake as well as providing validation for numerical tools.

### NFA

The agreement between NFA predictions and laboratory measurements is good. Since NFA uses free-slip conditions on the hull, the good agreement suggests that the wall boundary layer does not affect wave breaking and air entrainment in the transom region when the Reynolds number is sufficiently high. Analysis of the air entrainment suggests that the peaks that are observed in the spectra of the free-surface elevation in the transom region are due to the effects of a multi-phase shear layer that forms beneath the rooster tail and continues into the stern breaking wave. In terms of processing data, one advantage of the numerical simulations over laboratory measurements is that all of the data is readily available. NFA predictions of drag, free-surface elevations, and air entrainment are all within experimental error. Without the experiments, there is no basis to validate the numerical simulations, and the development of computer codes such as NFA would not be possible. NFA's ease of use, numerical stability, rapid turn around, and high accuracy provide a robust framework for simulating complex flows around naval combatants. Future improvements to the NFA algorithm are only possible under the guidance of high-fidelity laboratory and field experiments such as those reported in this paper.

### CFDShip-Iowa V4

CFDShip-Iowa V4 mean and unsteady wave elevation predictions using DES are validated for a transom-stern model for 3.60 m/s (7 knots),  $F_r=0.38$  and 4.12 m/s (8 knots),  $F_r=0.43$ . The drag predictions are within 4.2% of the experimental results for both flow conditions. The grids are found to be sufficiently fine to properly activate LES in the transom region as resolved turbulent kinetic energy is greater than 92% of the total. The transom flow pattern compares well with those from the experiments, i.e., a wetted transom is predicted for 3.60 m/s (7 knots) with wide wake dominated by wave breaking up to the transom. The 4.12 m/s (8 knot) simulation predicts a dry transom with well-defined narrow wake that forms a rooster tail with breaking waves.

Comparison with the experimental results are reasonably good for the drag, mean wave elevation, wave-cuts and FFT, but coherent patterns are not observed for the RMS. CFDShip-Iowa V4 mean wave elevation and wave-cut predictions are within 4.5% and 6.5% of

the experimental results for the wetted and dry transom case, respectively. The larger errors for the dry transom case were due to the 18% under prediction of the diverging wave angle. CFDShip-Iowa V4 predictions show a shoulder wave close to the transom for both speeds, which are not observed in the LiDAR wave elevation cross-sectional profiles. The transom wave elevation dominant frequency for the wetted transom is predicted within 0.1% of that found from the experimental work, whereas neither results predict any dominant frequency for the dry transom. The comparison errors are reasonable and supports the credibility of CFDShip-Iowa V4 simulations.

The dominant wetted transom flow frequency is explained as a Karman-like vortex shedding from the transom bottom corner, as the frequencies are within 3%. The Karman-like shedding Strouhal number,  $S_t=0.075$ , is 33% lower than that for appended Athena and 8.5% higher than the upper limit of the Karman-like shedding range based on the Strouhal number,  $S_t=0.066-0.069$ .

### ACKNOWLEDGEMENTS

The Office of Naval Research supports this research under multiple Office of Naval Research contract vehicles as directed by Dr. L. Patrick Purtell (ONR Code 331), program manager. The authors would like to acknowledge the efforts of Susan Brewton, Connor Bruns, Michael Capitain, Lisa Minnick, Toby Ratcliffe, James Rice, Lauren Russell, and Don Walker from NSWCCD - Code 50, the NSWCCD Media Lab, Eric Terrill and Genivieve Lada from the Scrips Institute of Oceanography, UCSD, and David Jeon, Daeyoum Kim and Mory Gharib from the California Institute of Technology. The support of the Data Analysis and Assessment Center (DAAC) is gratefully acknowledged. DAAC members include Dr. Michael Stephens, Randall Hand, Paul Adams, Miguel Valenciano, Kevin George, Tom Biddlecome, and Richard Walters. Animations of NFA simulations are available at <http://www.youtube.com/waveanimations>. Science Applications International Corporation IR&D supported recent upgrades to the NFA algorithm. NFA predictions are supported in part by a grant of computer time from the Department of Defense High Performance Computing Modernization Program (<http://www.hpcmo.hpc.mil/>). NFA simulations have been performed on the SGI Altix ICE at the U.S. Army Engineering Research and Development Center (ERDC).

### References

- Beale, K., Fu, T., Wyatt, D., & Walker, D., "Free surface measurements of breaking waves using Quantitative

- Visualization (QViz),” Proceedings of the 29th American Towing Tank Conference, Annapolis, Maryland, 2010.
- Bhushan, S., Xing, T., Carrica, P., & Stern, F., “Model and full-scale URANS/DES simulations for R/V Athena resistance, powering and motions,” Proceedings of the 9th International Conference on Numerical Ship Hydrodynamics, Ann Arbor, Michigan, 2007.
- Bhushan, S., Xing, T., & Stern, F., “Vortical structures and instability analysis for Athena wetted transom flow with full-scale validation,” J. Fluid Eng., in preparation for publication.
- Brucker, K. A., O’Shea, T. T., Dommermuth, D. G., & Adams, P., “Numerical simulations of breaking waves – weak spilling to strong plunging,” Proceedings of the 28th Symposium on Naval Hydrodynamics, Pasadena, California, USA, 2010, to appear.
- Carrica, P., Wilson, R., & Stern, F., “An unsteady single-phase Level Set method for viscous free surface flows,” Int. J. Numer. Meth. Fluids, Vol. 53 (2), 2007, pp. 229–256.
- Dommermuth, D. G., O’Shea, T. T., Wyatt, D. C., Ratcliffe, T., Weymouth, G. D., Hendrikson, K. L., Yue, D. K., Sussman, M., Adams, P., & Valenciano, M., “An application of Cartesian-grid and volume-of-fluid methods to numerical ship hydrodynamics,” Proceedings of the 9th International Conference on Numerical Ship Hydrodynamics, Ann Arbor, Michigan, 2007.
- Dommermuth, D. G., O’Shea, T. T., Wyatt, D. C., Sussman, M., Weymouth, G. D., Yue, D. K., Adams, P., & Hand, R., “The numerical simulation of ship waves using Cartesian-grid and volume-of-fluid methods,” Proceedings of the 26th Symposium on Naval Hydrodynamics, Rome, Italy, 2006.
- Fu, T., Fullerton, A., & Drazen, D., “Free-surface measurements in a tow tank using LiDAR,” ASME 2009 Fluids Engineering summer meeting (FEDSM2009) forum on fluid measurements and instrumentation, Vol. FEDSM2009-78464, Vail, Colorado, 2009a.
- Fu, T., Fullerton, A., Drazen, D., Minnick, L., Walker, D., Ratcliffe, T., Russell, L., & Capitain, M., A Detailed Study of Transom Breaking waves: Part II, Technical Report NSWCCD-50-TR-2010/003, Naval Surface Warfare Center, Carderock, 2010.
- Fu, T., Fullerton, A., Ratcliffe, T., Minnick, L., Walker, D., Pence, M., & Anderson, K., A Detailed Study of Transom Breaking Waves, Technical Report NSWCCD-50-TR-2009/025, Naval Surface Warfare Center, Carderock, 2009b.
- Fu, T., Fullerton, A., Terrill, E., & Lada, G., “Measurements of the wave field around the R/V Athena I,” Proceedings of the 26th Symposium on Naval Hydrodynamics, Rome, Italy, 2006a.
- Fu, T., Rice, J., Terrill, E., Walker, D., & Lada, G., “Measurement and characterization of full-scale ship waves,” Ships and Ship Systems (S3) Tech. Symposium, Carderock, MD, USA, 2006b.
- Fullerton, A. & Fu, T., “Acoustic doppler current profiler (adcp) measurements of breaking waves,” ASME 2008 Fluids Engineering summer meeting (FEDSM2008) forum on fluid measurements and instrumentation, Vol. FEDSM2008-55313, Jacksonville, FL, 2003.
- Furey, D. & Fu, T., “Quantitative Visualization (QViz) Hydrodynamic measurement technique of multiphase unsteady surfaces,” Proceedings of the 24th Symposium on Naval Hydrodynamics, Fukuoka, Japan, 2002.
- Hunt, J., Wray, A., & Moin, P., Eddies, stream, and convergence zones in turbulent flows, Technical Report CTR-S88, Center for Turbulence Research, 1988.
- Jeon, D., Pereira, F., & Gharib, M., “Applications of defocusing DPIV to bubbly flow measurement,” Particle & Particle Sys. Char., Vol. 20, no. 3, 2003, pp. 193–198.
- Kandasamy, M., Xing, T., & Stern, F., “Unsteady free-surface wave-induced separation: vortical structures and instabilities,” J. Fluids and Structures, Vol. 25(2), 2008, pp. 343–363.
- Karion, A., Waniewski-Sur, T., Fu, T., Furey, D., Rice, J., & Walker, D., “Experimental study of the bow wave of a large towed wedge,” Proceedings of the 8th International Conference on Numerical Ship Hydrodynamics, Busan, Korea, 2003.
- Maki, K., Doctors, L., & Beck, R., “On the profile of the flow behind a transom stern,” 9th Int. Conf. on Num. Ship Hydrodynamics, Ann Arbor, Michigan, 2007.
- O’Shea, T. T., Brucker, K. A., Dommermuth, D. G., & Wyatt, D. C., “A numerical formulation for simulating free-surface hydrodynamics,” Proceedings of the 27th Symposium on Naval Hydrodynamics, Seoul, Korea, 2008.
- Pereira, F., Gharib, M., Dabiri, D., & Modarress, D., “Defocusing DPIV: A 3-component 3-D DPIV measurement technique,” Exp. Fluids [Suppl. S], Vol. 29, 2000, pp. S78–S84.
- Rice, J., Walker, D., Fu, T., Karion, A., & Ratcliffe, T., “Quantitative characterization of the free-surface around surface ships,” Proceedings of the 25th Symposium on Naval Hydrodynamics, St. John’s, Newfoundland and Labrador, Canada, 2004.
- Rodríguez-Rodríguez, J., Marugán-Cruz, C., Aliseda, A., & Lasheras, J., “Dynamics of large turbulent structures in a hydraulic jump,” J. Fluid Mech., submitted.
- Rottman, J. W., Brucker, K. A., Dommermuth, D. G., &

- Broutman, D., "Parameterization of the internal-wave field generated by a submarine and its turbulent wake in a uniformly stratified fluid," Proceedings of the 28th Symposium on Naval Hydrodynamics, Pasadena, California, USA, 2010, to appear.
- Waniewski, T., Air entrainment by bow waves, Ph.D. thesis, California Institute of Technology, 1999.
- Wehausen, J., "Effect of the initial acceleration upon the wave resistance of ship models," J. Ship Research, Vol. 7(3), 1964, pp. 38–50.
- Wilson, R., Carrica, P., & Stern, F., "URANS simulation for a high-speed transom-stern ship with breaking waves," Int. J. CFD, Vol. 20(2), 2006, pp. 105–125.
- Wyatt, D., Fu, T., Taylor, G., Terrill, E., Xing, T., Bhushan, S., O'Shea, T., & Dommermuth, D., "Comparison of full-scale experimental measurements and computational predictions of the transom-stern wave of the R/V Athena I," Proceedings of the 27th Symposium on Naval Hydrodynamics, Seoul, Korea, 2008.